

LBT IR observations of candidate super-Eddington quasars

T. M. Buendia-Rios¹, P. Marziani², C. A. Negrete³ and D. Dultzin¹

¹ Instituto de Astronomía, UNAM, México CDMX. 04510, Mexico

² INAF, Osservatorio astronomico di Padova, 35122, Padova, Italy

³ CONACyT Research Fellow - Instituto de Astronomía, UNAM, México CDMX. 04510, Mexico

Accepted XXX. Received YYY; in original form ZZZ

ABSTRACT

Quasars accreting at very high rates are believed to be prime movers of galactic evolution because of their high radiative and mechanical output. The study presented in this paper investigates a sample of six highly accreting quasars at redshifts $z = 2 - 3$ using near-infrared observations from the LUCI spectrograph at the Large Binocular Telescope (LBT). The aim is obtain a precise measure of the quasar systemic redshift and accretion parameters (black hole mass and Eddington ratio) primarily from the $H\beta$ line, and on second stance from other intermediate and low ionization lines. Outflow dynamical parameters (mass rate of outflowing gas, its kinetic power and momentum rate) were estimated from the $C\text{IV}\lambda 1549$ emission line that is perhaps the most easily accessible tracer of high-ionization winds from the accretion disk, obtained from the Sloan Digital Sky Survey. In addition, the joint analysis of the rest-frame optical and UV spectra allowed us to estimate the chemical composition of the broad line emitting gas. The high metal content of the outflowing gas ($Z \gtrsim 10Z_{\odot}$) and the high values of thrust and kinetic power may induce a chemical feedback effect in the quasar host, in addition to mechanical feedback.

Key words: quasars: supermassive black holes – quasars: emission lines – line: profiles – line: formation

1 INTRODUCTION

Highly accreting quasars are the most luminous quasars for a given black hole mass (Mineshige et al. 2000; Ohsuga et al. 2005; Ohsuga & Mineshige 2007; Sadowski 2011). They may be among the prime agents of galactic evolution (e.g., Hopkins et al. 2006; Fabian 2012) because of their extreme radiative and mechanical output: nuclear outflows, and radiative feedback effects on their host galaxies, are maximized and reach impressive values of kinetic power and momentum rate (e.g., Marziani et al. 2016; Vietri et al. 2018). Very luminous quasars radiating close to the Eddington limit do not exist anymore in the local Universe (e.g., Shankar et al. 2004, 2009), but were relatively frequent at $z \approx 2$, an epoch where also the volume integrated star formation rate reaches its peak (Conselice 2014, and references therein). Therefore, quasar feedback effects that may be more relevant for galactic evolution should be studied at relatively high z .

A signature of quasar outflows is the Doppler shifting toward the blue of absorptions and emission lines (e.g. Marziani & Sulentic 2012). The $C\text{IV}\lambda 1549$ line in emission is observed in almost every quasar spectrum, is prominent ($W \sim 5 - 200\text{\AA}$), relatively clear from contaminant lines, and is often – but not always – significantly blueshifted with respect to rest frame (e.g., Marziani et al. 1996; Leighly 2004; Leighly & Moore 2004; Sulentic et al. 2007; Richards et al. 2011; Marziani et al. 2016; Vietri et al. 2020). The $C\text{IV}\lambda 1549$ line profile is perhaps the most accessible diagnostics of nuclear outflows (i.e., traces the outflow at the origin, as an accretion disk wind) in quasars at $z > 1.4$, where $C\text{IV}\lambda 1549$ shifts to the optical range. For this reason, the quasar rest-frame (RF) has to be measured with high precision ($< 100 \text{ km s}^{-1}$ at 1σ confidence level) in order to estimate the dynamical parameters of the wind (such as mass

flow rate, thrust and kinetic power) that may be able to escape the black hole sphere of influence. To reliably set the quasar RF, low-ionization narrow lines such as the narrow component of $H\beta$ are best suited (Eracleous & Halpern 2004; Bon et al. 2020), as recent work confirms that it is not possible to obtain accurate redshift estimates from broad UV lines, especially from the ones whose parent species ionization potential is high (Sulentic et al. 2007; Hewett & Wild 2010; Shen 2016).

We remark that the FWHM of $H\beta$ is an appropriate virial broadening estimator for the computation of the black hole mass (Mejia-Restrepo et al. 2016, and references therein), while $C\text{IV}\lambda 1549$ line is unsuitable especially for sources radiating at high Eddington ratio (Sulentic et al. 2007; Netzer et al. 2007; Richards et al. 2011; Marziani et al. 2019), as the broadening is most likely due to a velocity shear and not to virialized gas motion. Even if a correction to the line width can be applied (Brotherton et al. 2015; Coatman et al. 2016; Marziani et al. 2019), the process is often cumbersome and may still require an independent estimate of the quasar rest frame to work at best. Other low-and intermediate ionization lines such as $\text{MgII}\lambda 2800$ (Trakhtenbrot & Netzer 2012; Marziani et al. 2013a) and $\text{AlIII}\lambda 1860$ (Marziani et al. 2022) need further testing, because an outflow component has been revealed in both lines for highly-accreting sources (Marziani et al. 2013b).

One can now count on the improved ability to distinguish sources radiating close to the Eddington limit, thanks to the exploitation of E1 of quasars (E1, e.g. Boroson & Green 1992; Sulentic et al. 2000; Shen & Ho 2014). However, there are still relatively few observations covering $H\beta$, [OIII], and FeII redshifted into the IR for highly accreting quasars (hereafter xA, for extreme Population A, Marziani & Sulentic 2014). An empirical selection criterion is based

on the value of the ratio between the singly-ionized blend centered at $\lambda 4570$ and the Balmer line $H\beta$. A source is highly accreting if $R_{\text{FeII}} \gtrsim 1$ (Marziani & Sulentic 2014; Du et al. 2016). Sources at low z meeting this selection criterion are mostly radiating close or above Eddington ratio $L/L_{\text{Edd}} \approx 1$ (Marziani & Sulentic 2014; Du et al. 2016; Negrete et al. 2018).

Criteria have been suggested to select sources radiating close to their Eddington limit from diagnostic ratios computed from UV lines (Marziani & Sulentic 2014), as outlined in Section 2. However, the selection criterion based on UV ratios is as yet untested on large samples. This circumstance is unfortunate, as it makes the identification of highly accreting sources more prone to spurious classification. In addition, other properties need confirmations. Among all, the high value of the metallicity inferred by several previous studies (Śniegowska et al. 2020) can be more safely verified if ratios involving $\text{MgII}\lambda 2800$, $\text{Fe II}_{\text{opt}}$ and $H\beta$ are available (Floris et al. 2024). As mentioned, highly accreting quasars should produce the highest radiative output per unit black hole mass. Even if radiation pressure drives a wind, estimates of the wind dynamical parameters as traced by the optical and UV high-ionization lines differ wildly (e.g., Bisogni et al. 2017; Fiore et al. 2017; Marziani et al. 2017; Vietri 2017; Vietri et al. 2018; Kakkad et al. 2020), the wind dynamical parameters of xA sources at the highest luminosity should exceed the threshold for significant feedback effect (Di Matteo et al. 2005), if AGN are to have a feedback effect at all. This is said leaving aside the most complex part of the problem, namely the dispersion of thrust and kinetic power along the interstellar medium (King & Pounds 2015).

The coverage of the $H\beta$ spectral range is essential for verifying the consistency of the UV/optical selection criteria, conducting additional tests at high z values, and analyzing the dynamical parameters of the winds. However, there is still a lack of data covering the optical/UV range at high redshifts, especially for super-Eddington candidates. The LBT sample makes a significant contribution to the study of xA quasars by expanding the observational coverage available to date (available for a few tens of sources at most), and providing useful information of the physical properties, emission mechanisms, and evolutionary trends regarding the highly accreting sources. After the description of the sample selection in Section 2, Section 3 presents the new LUCI (LBT Utility Camera in the Infrared, Seifert et al. 2003) NIR observations at LBT that, as summarized before, are fundamental to measure the dynamical properties of the wind from the accretion disk as they relate them to the accretion parameters. Section 4 describes the analysis of the redshift estimation, the multi-component fitting of the $H\beta$ and FeII spectral ranges, and the UV-RF from $\text{CIV}\lambda 1549$ to $\text{MgII}\lambda 2800$. In Section 5 we present the empirical results, including the inter-comparison between CIV and $H\beta$ and other lines. Section 6 is focused on the analysis of the derived physical parameters, and discusses the virial M_{BH} obtained from $H\beta$, $\text{MgII}\lambda 2800$ and $\text{AlIII}\lambda 1860$. Wind parameters including mass outflow rate, thrust, kinetics power, estimates of metal content, and the inclusion of these objects in an Hubble diagram are also discussed.

2 SAMPLE DESCRIPTION AND OBSERVATIONS

2.1 Selection of xA quasars

As the sample for the NIR (using LUCI observations), we selected six sources among the ones of the Marziani & Sulentic (2014) SDSS-based sample in the redshift range $2.35 < z < 2.44$ in order to ensure

maximum S/N and full coverage in the $H\beta$ spectral range $4600 \text{ \AA} - 5100 \text{ \AA}$. $\text{CIV}\lambda 1549$, $\text{AlIII}\lambda 1860$ and $\text{SiIII}\lambda 1892$ are already covered by high S/N optical spectra from the Sloan survey.

A previous analysis (MS14) suggested working criteria to identify highly accreting quasars (i. e. extreme quasars or 'xA' quasars): (a) intensity ratio between FeII emission at $\lambda 4570$ (or equivalently at $\lambda 5130$) and $H\beta$ $R_{\text{FeII}} > 1.0$, in the optical; (b) intensity ratios $\text{AlIII}\lambda 1860 / \text{SiIII}\lambda 1892 \geq 0.5$ and $\text{SiIII}\lambda 1892 / \text{CIII}\lambda 1909 \leq 1.0$, in the UV. The sources of MS14 shown Eddington ratio distribution of low- z and high- z highly accreting objects is sharply peaked around 1, with a dispersion of just 0.13 dex, and were selected by applying criteria (a) and (b). The sources of the present sample were selected for observations by applying criteria (b) only due to the lack of pre-existing IR observations covering the $H\beta$ spectral range.

Table 1 gives source identifications and basic properties including: the SDSS name (Col. 1), apparent V magnitude (Col. 2), apparent magnitudes in the H-band obtained from 2MASS and LUCI-LBT (Col. 5), redshift and uncertainty (Cols. 6 and 7), airmass (Col. 8) and comments (Col. 9). Three of the sources of our sample are radio-detected in the Faint Images of the Radio Sky at Twenty-cm Survey (VLA-FIRST Survey¹), and were found to be formally radio-quiet, although close to the minimum Kellermann's ratio for radio-intermediate $R_K \sim 10$ (Zamfir et al. 2008). The R_K reported in Table 1 was computed according to the original definition by Kellermann et al. (1989), by taking the FIRST flux and dividing it by the H band flux which correspond to the de-redshifted 5 GHz and B band fluxes.

2.2 Preliminary analysis of Sloan data

The optical data were acquired through the Baryon Oscillation Spectroscopic Survey (BOSS), the extended Baryon Oscillation Spectroscopic Survey (eBOSS), and the Legacy Survey programs of the Sloan Digital Sky Survey (SDSS). The spectra, which had been calibrated for both wavelength and flux, serve as the optical counterpart to the NIR sample. For redshift and flux conversions to the rest frame, we divided the wavelength scale by $(1+z)$ and increased the flux by a factor of $(1+z)^3$, using the redshift values provided by SDSS as initial estimates.

3 LUCI/LBT OBSERVATIONS AND DATA REDUCTION

Table 2 contains a summary of the observations, including the SDSS identification, observation date, grism employed, total exposure time, and the camera employed for each LUCI configuration. The observations required the LUCI1 N1.8 camera with a plate scale of 0.25 pixels and the 210 lines/mm high-resolution grating, covering the H band (central wavelength $1.65 \mu\text{m}$) for each run. For the grism, it was employed G210HiRes and G200LoRes with resolutions of 5900 and 1900/2600 $[\lambda_{\text{cen}}/\delta\lambda]$, respectively. The λ_{cen} were 1.65 and $1.93 \mu\text{m}$ for the high-resolution grism and low, respectively.

The calibration strategy and requirements include standard stars for spectrophotometric calibration and telluric band subtraction, which were deemed necessary for each target. These calibrations were to be conducted at a similar airmass as the science exposure (~ 1.5), either immediately before or after the science exposure (seeing requested $1.5[\text{arcsec}]$). The exposure time for each calibration was set at 3-5 minutes, suitable for a typical star with a magnitude of $r \sim 10$. Consequently, the total exposure time on each target comprised

¹ <https://sundog.stsci.edu/index.html>

Table 1. Source identification and basic properties of the LUCI-LBT sample.

SDSS ID (1)	m_V (2)	i_{SDSS} (3)	z_{SDSS} (4)	$H_{2\text{MASS}}$ (5)	z_{sys} (6)	δz_{sys} (7)	AM (8)	Comments (9)
J084502.73+081214.3	18.357	18.280	18.048	16.862	2.37104	0.00077	1.67	RE: 1.49 ± 0.13 mJy, $R_K \approx 8$ BAL QSO
J093403.96+315331.3	17.166	17.111	16.869	15.01*–14.68*	2.42368	0.00026	1.47	RE: 4.68 ± 0.13 mJy, $R_K \approx 3.5$ FBQS BAL
J105427.17+253600.8	17.361	17.644	17.361	16.126	2.41429	0.00057	1.09	RE: 2.99 ± 0.13 mJy, $R_K \approx 8$ FBQS BAL
J125914.83+672011.8	17.983	17.947	17.776	16.257	2.44480	0.00051	1.45	
J144218.09+484101.8	18.800	18.798	18.629	...	2.43337	0.00013	1.42	$< z - H > \approx 1.28 \pm 0.14$ $\rightarrow H \approx 17.35$
J210831.56-063022.5	17.234	17.176	17.064	15.775	2.37180	0.00031	1.67	

Notes: Columns are as follows: (1) SDSS coordinate name. (2) Apparent V magnitude. (3) SDSS magnitude in the i band. (4) SDSS magnitude in the z band. (5) Apparent IR magnitude in the H-band (2MASS), *Apparent magnitude in the H-band using our LBT estimates. (6) Systemic redshift. (7) Redshift uncertainty. (8) AM = airmass. (9) Quasar classification: first bright quasar survey (FBQS); broad absorption lines (BAL); radio emission (RE) detected in FIRST; R_K is Kellermann's ratio (Kellermann et al. 1989).

approximately 1–3 hours ($3\text{--}5 \times 2$ for telluric and spectrophotometric calibration \times number of observations).

Data reduction was carried out in a standard way using the Image Reduction and Analysis Facility (IRAF, Tody 1986). Bias subtraction correction was performed nightly. Sequence of frames with a given detector integration time were obtained with the source at different positions (e.g. A,B) along the slit. Spectra were taken as a sequence of exposures recorded at A and B position. Wavelength calibration was obtained using the night-sky spectral emission lines from Rousset et al. (2000), and the spectra were corrected for dispersion direction/CCD frame axis and geometric distortion using the IRAF tasks `rotate` and `transform`. The A and B calibrated 2D spectra were then subtracted one to the other. 1D spectra were traced on the difference frame, and then re-subtracted.

Instrumental response and specific flux calibration were obtained nightly with observations of the spectrophotometric standard stars (see Table 2). Telluric absorptions, that affect our spectra, were also corrected using the standard stars and IR stellar spectra from Pickles (1998), to obtain a normalized wavelength-calibrated template of the absorption features. Each target spectrum was then divided by its corresponding standard star spectrum in order to correct for the atmospheric absorption features. This was achieved with the `telluric` task, which allows to optimize the correction with slight adjustments in shift and scaling of template of the absorption features. Finally, the correct flux calibration of each spectrum was achieved by scaling it according to the magnitude of the standard star and the source divided by the integration time. For this, we used the `sbands` task. The standard stars were observed with a wider slit than the sources, so significant light loss occurred. We compared our estimates with the Two Micron All Sky Survey (2MASS, Skrutskie et al. 2006) magnitudes for our spectra. If we encountered differences $> 1.5\text{mag}$, we employed the values from 2MASS. In Table 1, the only source that was calibrated with our LBT estimates is J093403.96, and we present two values corresponding to each camera data, as this object was observed in fraternal mode.

4 DATA ANALYSIS

4.1 Redshift estimations

We found that the narrow component of $H\beta$ and the $[\text{OIII}]$ emission are very weak in our spectra, in accordance with the results that broad $H\beta$ is mainly affected close to the line base in highly accreting sources (Negrete et al. 2018). Redshifts were measured using the wavelength of the $H\beta$ peak intensity, with `splot` task from IRAF. A posteriori cross-check towards the redshift derived from $H\beta$ with the ones of $\text{MgII}\lambda 2800$ and $\text{AlIII}\lambda 1860$ was done, and a good agreement was found. The redshift estimates are reported for each object in Table 1.

4.2 Multi-component fitting

To analyze the emission lines of the spectra, multi-component fits were carried out using the task `specfit` (Kriss 1994). This routine allowed us to simultaneously fit all the components present in the spectrum: continuum, FeII features, and emission lines, computing the χ^2 parameter that measures the difference between the original spectra and the fitted one. The task `specfit` minimizes the χ^2 to find the best fit.

The primary continuum source in the optical-UV region is well known to be originated from the accretion disk (e.g., Malkan & Sargent 1982; Wandel & Petrosian 1988; Capellupo et al. 2016). In the absence of extinction, the most widely-used model for the continuum is a single power-law over a limited spectral range (see e.g., Śniegowska et al. 2020). In Fig. 1 are shown the quasar spectra with the coverage from the LBT and SDSS observations. We fitted a local continuum for the spectral ranges centered on the most important emission lines shown in Fig. 1: 1400\AA blend, $\text{CIV}\lambda 1549$, 1900\AA blend, $\text{MgII}\lambda 2800$, and $H\beta$, using a single power-law for each range centered in 1350, 1700, 3050, and 5100\AA , respectively.

4.2.1 Region 1: 1250–1450 \AA .

The dominant emission in this region involves $\text{SiIV}\lambda 1397 + \text{OIV}\lambda 1402$ (the 1400\AA blend), and is accompanied by weaker $\text{SiII}\lambda 1263$, $\text{SiII}\lambda 1306$, $\text{OIII}\lambda 1304$, and $\text{CII}\lambda 1335$.

Table 2. Log of observations

ID (1)	Obs. Date (2) (3)		Grism (4)	ET (5)	Camera (6)	Standard Star (7)	Comments (8)
J084502	2017-04-18	2011-11-28	G210HiRes	1560	LUCI1	HIP41751 (G4V)	seeing=0.7 -0.9
	2017-04-18		G210HiRes	1560	LUCI2		fraternal mode
J093403	2019-01-27	2018-12-11	G200LoRes	1440	LUCI1	HIP 44027 (G2V)	
	2019-01-27		G200LoRes	1440	LUCI2		fraternal mode
J105427	2016-12-04	2013-02-17	G210HiRes	1800	LUCI1	HIP 52192 (G2V)	seeing=1.7 - 3.2
J125914	2017-04-17	2014-04-01	G210HiRes	1800	LUCI1	HIP64451 (F7V)	
	2017-04-17		G210HiRes	2320	LUCI2		fraternal mode
J144218	2017-06-13	2013-04-13	G210HiRes	2900	LUCI2	HIP71172 (A0V)	
J210831	2016-09-17	2001-06-21	G210HiRes	1440	LUCI1	HIP 106382 (A0V)	seeing=0.49-0.65

Notes: Columns are as follows: (1) SDSS identification. (2) LBT Observation Date; (3) SDSS Observation Date. (4) Grism. (5) Exposure time (ET) in seconds. (6) Camera used, LUCI configuration. (7) Standard star used, obtained from our LBT observations and extracted from [Pickles \(1998\)](#); spectral type is specified in parenthesis.

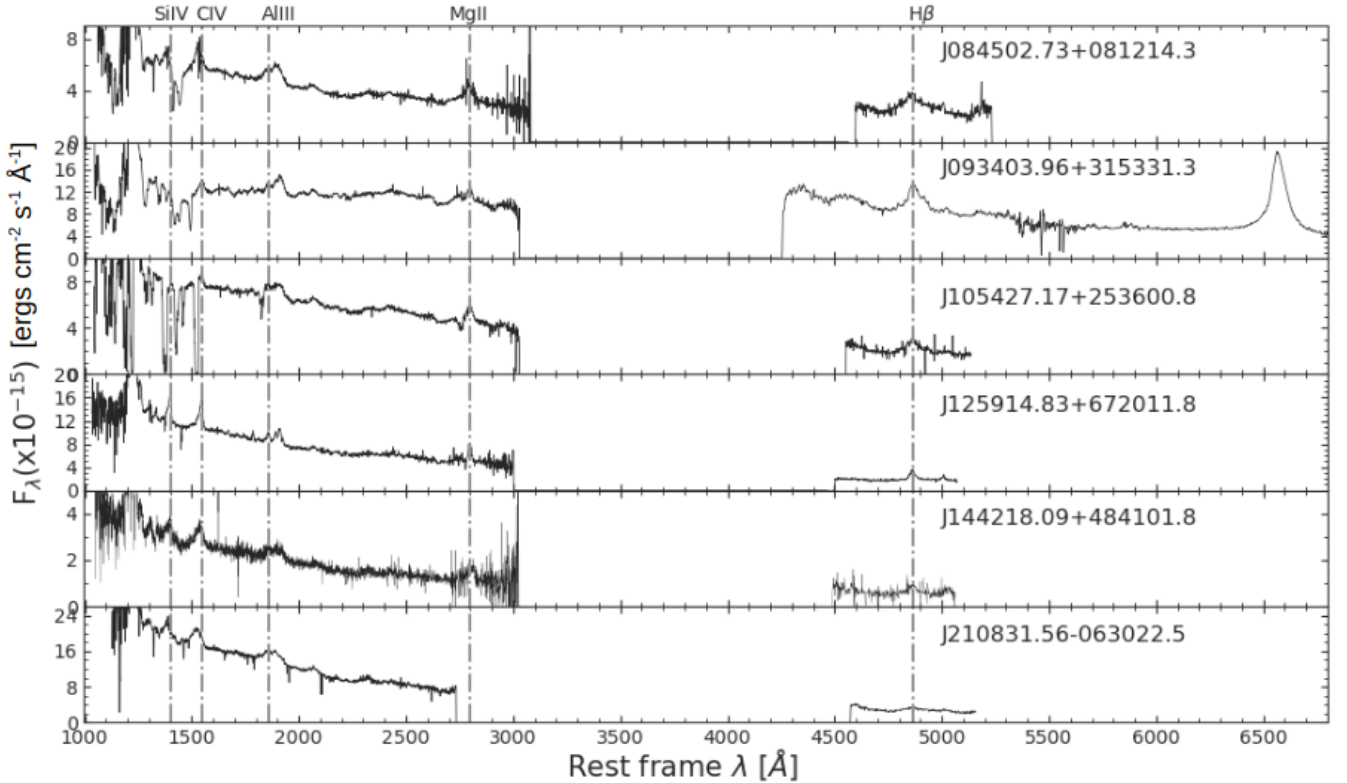


Figure 1. Rest-frame spectra of our six type 1 AGN, with UV and optical regions after joining the observed spectra from LBT and the SDSS. Abscissas are rest-frame wavelength in Å and ordinates are specific flux in units of $10^{-15} \text{ ergs s}^{-1} \text{ cm}^{-2} \text{ Å}^{-1}$. Dot dashed vertical lines trace the rest-frame wavelength, from left to right, of SiIV 1397, CIV 1549, AlIII 1860, MgII 2800, and Hβ, respectively.

Sirv 1397+Orv 1402 – The underlying assumption of the blend modeling is that the broad component (BC) emission is dominated by Sirv 1397 due to collisional deexcitation of the inter combination Orv 1402 multiplet ([Wills & Netzer 1979](#)), while the blue shifted component is due to an inextricable contribution of both Orv 1402+ Sirv 1397. The continuum is fitted with a single power-law in the region 1450-1700 Å, using a continuum window at 1700 Å as defined by [Francis et al. \(1991\)](#). The Sirv 1397+Orv 1402 feature is a high-ionization blend, and shows a blueshifted, asymmetric pro-

file not unlike C IV. The broad component was modeled with the same emission components of C IV, whenever possible. If the blue side of the 1400 Å blend was strongly contaminated by absorption features (J0934 and J1054) only the line flux was free to vary but the blueshifted Sirv 1397+Orv 1402 emission was modeled still taking the parameters of the asymmetry, width, and profile of C IV Blue component. The S/N between 30 and 40 always allows for the deblending of the broad and blue components when the blend is covered by the SDSS spectra.

4.2.2 Region 2: 1450-1700Å.

The C IV $\lambda 1549$ emission line dominates this region and is accompanied by He II $\lambda 1640$, O III $\lambda 1663$ and Al III $\lambda 1670$. We followed the method of [Martínez-Aldama et al. \(2018\)](#).

C IV $\lambda 1549$ – The BC of C IV is modeled by a Lorentzian profile fixed at the rest-frame. The flux of the C IV BC is free to vary and FWHM is assumed to be the same or larger as Al III $\lambda 1860$ and Si III $\lambda 1892$. All the C IV profiles in our sample show a blueshift and or blueward asymmetry. In order to model it with `specfit`, we used one or two blueshifted skewed Gaussian profiles. The flux, FWHM, asymmetry, and shift were unconstrained.

He II $\lambda 1640$ – We assumed a profile similar to the one of C IV $\lambda 1549$: Lorentzian and skewed Gaussian profiles for the BC and blueshifted components, respectively. The FWHM, shift and asymmetry were assumed equal to those of C IV $\lambda 1549$, but the flux varies freely.

O III $\lambda 1663$, Al III $\lambda 1670$ – Components modeled with unshifted Lorentzian profiles with their fluxes and FWHM varying freely.

4.2.3 Region 3: 1650-2150Å.

In the 1900Å blend, the most prominent emission lines are: Al III $\lambda 1860$, Si III $\lambda 1892$ and C III $\lambda 1909$. We followed the considerations made by [Buendia-Rios et al. \(2023\)](#).

Fe II and Fe I – Emission of the Fe II multiplets can be strong in the vicinity of C III $\lambda 1909$, as seen in the average quasar spectrum from [Vanden Berk et al. \(2001\)](#). They appear to be strong when Al III is also strong ([Hartig & Baldwin 1986](#); [Martínez-Aldama et al. 2018](#); [Mediavilla et al. 2019](#); [Temple et al. 2020](#)). We adopted the Fe II template model obtained by [Vestergaard & Wilkes \(2001\)](#). The `specfit` task scaled and broadened the template to reproduce the observed emission ([Boroson & Green 1992](#)). We fitted the multiplet Fe II UV191 (seen in the blueward of the 1900Å blend, [Moore 1945](#)) as an isolated Gaussian in the rest-frame. An extra component is added: Fe II $\lambda 1914$ to fit an excess seen near the red wing of C III $\lambda 1909$ associated with unresolved Fe II template emission ([Negrete et al. 2012](#)). This Fe II $\lambda 1914$ emission is a fitted using a Lorentzian profile to be consistent with the profile of the BCs ([Negrete et al. 2012, 2013](#)). This criterion rests on the assumption that Fe II $\lambda 1914$ and the Fe II UV multiplet #191 are enhanced by Ly α fluorescence ([Sigut & Pradhan 1998](#); [Johansson et al. 2000](#)).

C III $\lambda 1909$ – The BC is modeled by a Lorentzian profile fixed at the rest-frame, same as Si III $\lambda 1892$ and Al III $\lambda 1860$. Strengths and FWHM were left free to vary in the `specfit` model with one restriction: $\text{FWHM}(\text{C III } \lambda 1909) \leq \text{FWHM}(\text{Al III } \lambda 1860)$ or $\text{FWHM}(\text{Si III } \lambda 1892)$.

Si III $\lambda 1892$, Al III $\lambda 1860$ – Strengths and FWHM were free to vary, with one restriction: $\text{FWHM}(\text{Si III } \lambda 1892) \geq \text{FWHM}(\text{C III } \lambda 1909)$. The Al III $\lambda 1860$ doublet was resolved and the blue component shifts, FWHM, and intensity were allowed to vary, with the red one tied to the blue by identical FWHM and fixed wavelength ratio. The ratio between the intensity of the red and blue component of the doublet was kept fixed 0.8 ([Laor et al. 1997](#)). Doublet total strengths were left free to vary. We also added a blueshifted skewed Gaussian profile. The flux, FWHM, asymmetry and shift were unconstrained.

4.2.4 Region 4: 2600-3050Å.

The Mg II $\lambda 2800$ emission line dominates in this region and is accompanied by Al III $\lambda 2670$, O III $\lambda 2672$, and Fe II emission. We followed the method of [Marziani et al. \(2013a\)](#).

Fe II and Fe I – [Bruhweiler & Verner \(2008\)](#) provides Fe II UV emission templates computed from cloudy simulations and using an 830 level model of the Fe⁺ ion. The [Bruhweiler & Verner \(2008\)](#) template results in a systematic flux excess near 2950Å. The excess of flux observed was fitted with Fe II UV emission at $\lambda\lambda 2937.5, 2970.5$. Fe I emission has been predicted by photoionization models ([Sigut et al. 2004](#)) and was suggested by previous observations (e.g. [Kwan et al. 1995](#); [Marziani et al. 2013a](#)).

Mg II $\lambda 2800$ – The doublet was resolved and the blue component shifts, FWHM, and intensity were allowed to vary, with the shorter wavelength (blue) one tied to the longer (red) one by identical FWHM and fixed wavelength ratio. Lorentzian profiles at rest-frame were employed for both components. The ratio between the intensity of the red and blue component of the doublet was kept fixed at 0.8 ([Marziani et al. 2013a](#)), and in some cases it was assumed to be equal ([Laor et al. 1997](#); [Vestergaard & Wilkes 2001](#)). The doublet total strengths were left free to vary. We also added a blueshifted skewed Gaussian profile. The flux, FWHM, asymmetry, and shift were unconstrained.

Al III $\lambda 2670$, O III $\lambda 2672$ Components modeled with unshifted Lorentzian profiles with their fluxes and FWHM varying freely.

4.2.5 Region 5: 4500-5200Å.

The dominant emission in this region is H β accompanied by [O III] $\lambda\lambda 4959, 5007$ and Fe II. The method we used was the one of [Negrete et al. \(2018\)](#).

H β : The BC is modeled by a Lorentzian profile fixed at rest-frame. We also added a blueshifted skewed Gaussian profile. The flux, FWHM, asymmetry and shift were unconstrained.

Fe II : We used the semi-empirical template by [Marziani et al. \(2009\)](#), obtained from a high-resolution spectrum of I Zw 1, with a model of the Fe II_{opt} emission computed by a photoionization code in the range of H β .

[O III] $\lambda\lambda 4959, 5007$: As for the narrow component (NC), we fitted this doublet with two Gaussians, considering the ratio of theoretical intensities of 1:3 ([Dimitrijević et al. 2007](#)), the same FWHM, and the same line shift. We added a second blueshifted semi broad component if necessary to the fit. We have cases with no detectable [O III] $\lambda\lambda 4959, 5007$ NC or semi-broad emission.

4.2.6 Error estimates

Data used in this analysis come from two different instruments yielding spectra with widely different S/N. In addition, the comparison is between emission lines, which are relatively strong ($W(\text{H}\beta) > 50\text{\AA}$) and ones of which are fainter in the UV ($W(\text{Al III}), W(\text{Si IV}), W(\text{He II}) \leq 10\text{\AA}$ in most cases). So, we used the quality parameter Q ([Marziani et al. 2022](#)). The uncertainties of parameter Q were estimated following a Bayesian approach with a likelihood function

(their Eq. A1) dependent on the specific flux (as a function of wavelength), the S/N over the spectra and the expectation values of the multi-component model using `specfit`. For a detailed description of the prior and posterior model parameters in the Q parameter see Appendix A of (Marziani et al. 2022). This parameter is defined as the ratio between the line equivalent width and its FWHM multiplied by the S/N measured on the local continuum fitted for each region. By multiplying the S/N by the ratio W/FWHM , a computation of the S/N is more appropriate for a line depending on its strength and width. The parameter Q is larger for sharp lines in spectra with high S/N in the continuum. Especially for large Q values, the scatter is relatively modest, and the relation between the parameter FWHM, flux, and shift and $\log Q$ can be written in a linear form, save for the fractional uncertainty of $\text{FWHM}(\text{AlIII})$ that is best fit by $\delta\text{FWHM}/\text{FWHM} \approx 1 / (a + b \log Q)$. Table 3 of Marziani et al. (2022, Appendix A) provides the coefficients a and b of the best fits along with the Q domain.

5 RESULTS

The results are presented starting from multi-component fits for each spectral region (Section 5.1), and measurements reported for each object, accompanied by a detailed description of the most significant emissions from each region, including the blue component detected in several lines. Section 5.2 provides the measurements of the line profile parameters for the most prominent lines considered in the analysis. In Section 5.3, we analyze the consistency of selection criteria in the optical and UV for the LBT sample.

5.1 Immediate Results

Figures 2 and 3 show the resultant fits to the line profiles. From left to right $\text{SiIV}\lambda 1397$, $\text{CIV}\lambda 1549$, $\text{AlIII}\lambda 1860$, $\text{MgII}\lambda 2800$, and $\text{H}\beta$, respectively, for each source. In two cases, we could not make a good fit due to absorption contamination in the 1400Å blend: J093403.96+315331.3 and J105427.17+253600.8. As for the case of J210831.56-063022.5 $\text{MgII}\lambda 2800$, the data were not available in the SDSS. Table 3 lists, in the following order: identification by the SDSS name, rest-frame flux, equivalent width (W), FWHM, and R_{FeII} of the $\text{H}\beta$ BC line. The following columns report the $\text{H}\beta$ Blue parameters: rest-frame flux, W , FWHM, and shift. Here for shift we mean the radial velocity of the line peak with respect to the RF. The lower panels in Figs. 2 and 3 show the residual of the subtraction of the model spectrum from the observed one (solid black line). This residual was processed using a boxcar filter with a width of 10 pixels. The filtered residual was then subtracted from the original residual, and the resulting difference was defined as noise. The noise was quantified as the RMS computed over a 10-pixel windows, yielding the noise vector at the continuum level (red dashed line). The application of the boxcar filter offers the advantage of removing features that do not correspond to random noise but instead arise from systematic discrepancies between the model and the observed spectrum. Tables 4 and 5 also describe the SDSS name rest-frame flux, W , and FWHM of each emission line, including for the Blue parameters (if present). All uncertainties are computed using the quality parameter Q (Marziani et al. 2022). Uncertainties of the continuum windows fluxes were estimated with $\pm 1\sigma$ along the local continuum.

5.1.1 1400 Å blend

As previously mentioned, for J093403 and J105427 it was impossible to save the SiIV spectra due to significant absorptions contaminating the line profiles. Even in cases where the regions were available, absorptions were still present, making it somewhat challenging to accurately fit the emission of $\text{SiIV}+\text{OIV}$. In almost all cases, we had to account for these absorptions in the `specfit` multi-component model and statistically choose the best fits. In all cases, the dominant line profile (or at least similar to the BC) is the Blue component (FWHM up to 10,000 km/s). Only in the case of J125914 the converse is true, still with an asymmetrical BLUE line profile but with a dominant core component.

5.1.2 CIV

The scenario observed for CIV is similar to the blend 1400Å for the sources J0845, J0934, and J1054. Sources J0845 and J1054 have been classified as BAL quasars. For J0845 the BAL trough may affect more $\text{SiIV}\lambda 1397+\text{OIV}\lambda 1402$, while for $\text{CIV}\lambda 1549$ the BAL trough extends beyond the limit of the blueshifted emission component, making possible a reliable estimate. The absorption trough of J1054 is more complex. Only the trough beyond the blue end of the emission component was included in the fit. However, the sharp profile of the absorption between 1505 and 1540, and the lack of other absorptions affecting the CIV emission profile, made it possible to interpolate across the range affected by the absorption (Fig. 2), and retrieve a reliable CIV blueshifted component.

Among the quasars displaying an asymmetrical profile in the blue component are J0845, J1442, and J1259. The last one is exhibiting a particularly pronounced asymmetry attributed to the narrow profile in the BCs observed in all prominent emission lines. The FWHM values of the blue component are large, $\sim 10,000 \text{ km s}^{-1}$, except in the case of J0934 where $\text{FWHM} \approx 5030 \text{ km s}^{-1}$, still a large value among quasar outflows (Bisogni et al. 2017; Sulentic et al. 2017; Vietri et al. 2018, 2020).

5.1.3 1900 Å blend

In general, the S/N ratio was good (40-50) in the range of the 1900 Å blend, and the only source that exhibits significant absorptions is J105427. In this case, the absorption components were incorporated into the `specfit` model. The mean FWHM values are: $\text{CIII} \approx 3420 \text{ km s}^{-1}$, $\text{SiIII} \approx 3730 \text{ km s}^{-1}$, and $\text{AlIII} \approx 4153 \text{ km s}^{-1}$. All sources save two exhibit a strong blue component: weaker in the case of J1442, and absent for J1259. The FWHM of the AlIII Blue component is $\sim 5000 \text{ km s}^{-1}$, except for J210831, which has a higher value ($\sim 6600 \text{ km s}^{-1}$). For this region, it is possible to observe the significant contribution of FeII emission, which extends across the entire pseudo-continuum due to FeII and FeIII. Additionally, it is apparent that at around 2050Å, there is some emission not being accounted for by resonance lines, and instead attributed to FeII and FeIII (Vestergaard & Wilkes 2001; Martínez-Aldama et al. 2018; Mediavilla et al. 2018, 2019; Temple et al. 2020).

5.1.4 MgII

The spectra of J084502 and J144218 exhibited a low S/N (< 3), which complicated the fitting process for the redward wavelengths. However, for the remaining objects, the fitting quality was satisfactory. As mentioned earlier, the MgII spectrum for J2108 was not available in the SDSS. Only in the case of J1054 were absorption components

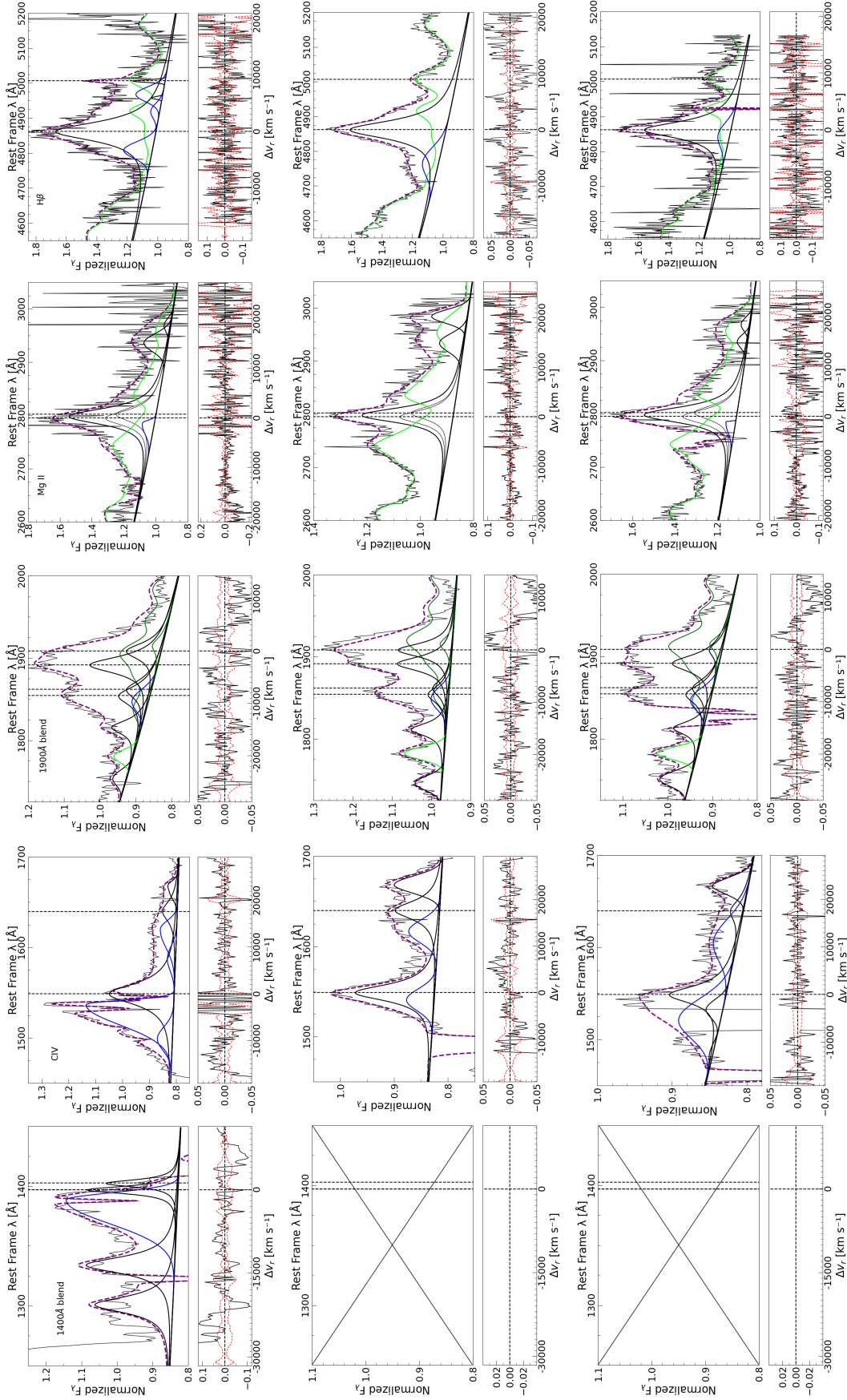


Figure 2. Multi-component fits, from left to right, of the 1400Å blend, CIV 1549, 1900Å blend, Mg II 2800, and Hβ spectral regions as described in Sect. 4.2. From top to bottom SDSS quasars: J084502.73+081214.3, J093403.96+315331.3, and J105427.17+253600.8. The top abscissa scale is rest-frame wavelength in Å. The ordinate scale is the normalized flux. In all the panels, a continuous black line marks the broad component at rest-frame, while the blue one corresponds to the blueshifted component associated with each emission. Dot-dashed vertical lines identify the position at rest-frame of the strongest emission lines. Dashed purple line marks the fit model obtained by `specfit`. The Fe II and Fe I contributions are traced by dark and pale green lines respectively. The lower panels show the residuals between spectrum and specfit model (black line) and the noise at 1σ -level (see text for more details). The abscissa is in radial velocity units (km s^{-1}).

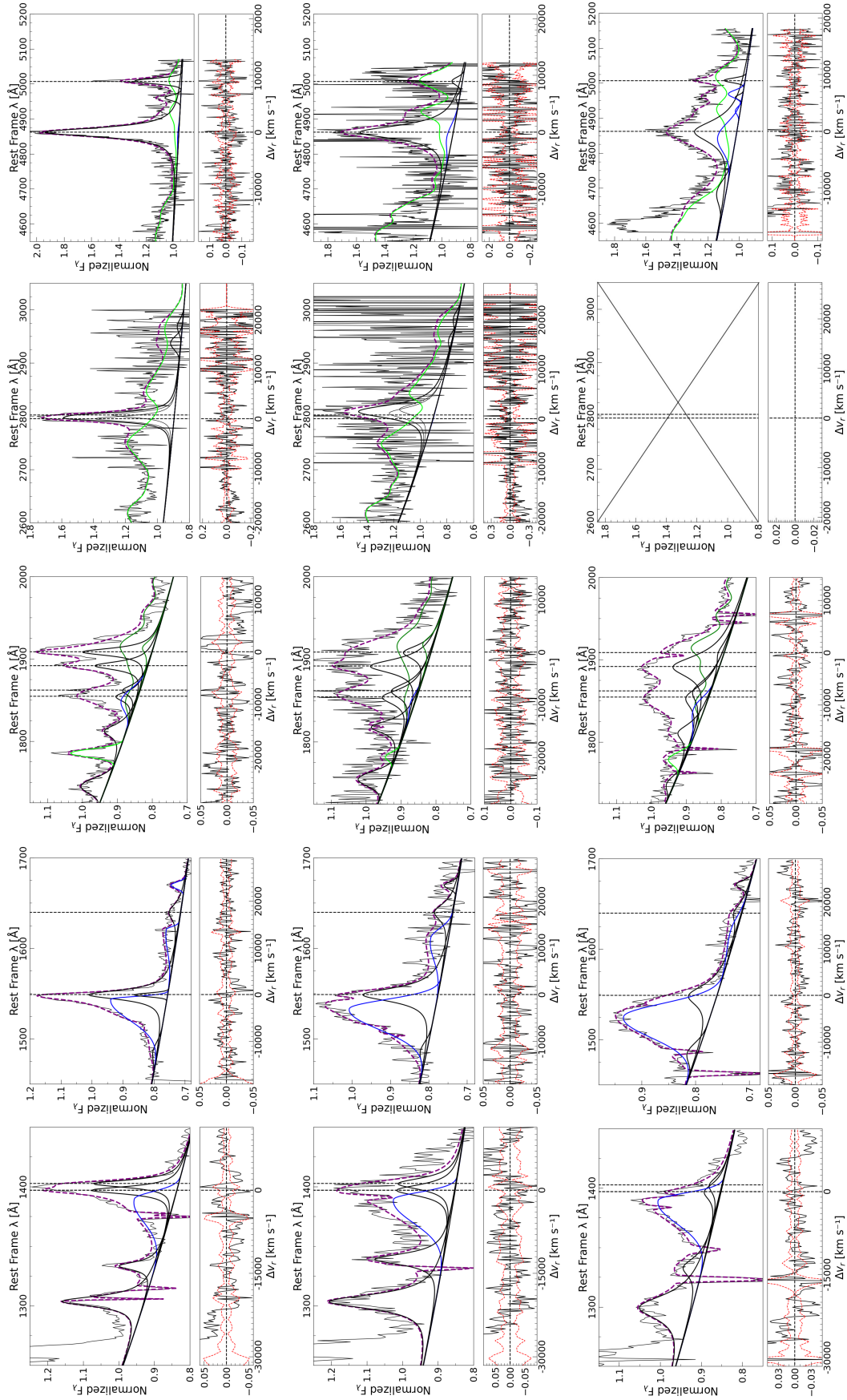


Figure 3. continued. From top to bottom SDSS quasars: J125914.83+672011.8, J144218.09+484101.8, and J210831.56-063022.5.

Table 3. Spectrophotometric Quantities of the H β components of this work.

Jcode	F $_{\lambda}$ (5100 Å)	H β BC			R $_{FeII}$		H β Blue			
		F	W	FWHM	BC	BC+Blue	F	W	FWHM	shift
(1)	(2)	(3)	(4)	(5)	(6)	(7)	(8)	(9)	(10)	(11)
J084502	207 \pm 12	14543 \pm 871	66 \pm 4	4193 \pm 503	0.784 \pm 0.06	0.717 \pm 0.07	2274 \pm 46	11 \pm 2	3422 \pm 274	-3151 \pm 36
J093403	772 \pm 5	49672 \pm 3463	61 \pm 4	4000 \pm 960	1.086 \pm 0.09	0.976 \pm 0.06	8332 \pm 49	11 \pm 1	5995 \pm 659	-5524 \pm 82
J105427	172 \pm 14	9203 \pm 736	50 \pm 4	3680 \pm 405	0.973 \pm 0.06	0.915 \pm 0.05	1144 \pm 18	7 \pm 0.2	4969 \pm 348	-732 \pm 12
J125914	172 \pm 10	8590 \pm 859	48 \pm 5	2000 \pm 300	0.464 \pm 0.05	0.483 \pm 0.08	-	-	-	-
J144218	53 \pm 12	2623 \pm 157	47 \pm 3	3000 \pm 270	1.407 \pm 0.07	1.398 \pm 0.06	174 \pm 7	3 \pm 0.1	5005 \pm 250	-779 \pm 23
J210831	226 \pm 11	7774 \pm 544	32 \pm 2	4982 \pm 498	1.588 \pm 0.18	1.124 \pm 0.12	2714 \pm 25	12 \pm 1	5975 \pm 478	-874 \pm 36

Notes: All measurements are in the quasar rest-frame, and line fluxes are all in units of 10^{-17} erg s $^{-1}$ cm $^{-2}$. Uncertainties are computed using the quality parameter Q defined by Marziani et al. (2022). Column (1): SDSS identification of the object. Column (2): Continuum Flux at 5100Å. Column (3): total flux of H β BC. Column (4): equivalent width of H β BC, in Å. Column (5): FWHM H β BC, in km s $^{-1}$. Columns (6, 7): R_{FeII} parameter with H β BC only and with full profile (i.e. BC+Blue). Columns (8) to (10): same as H β BC but for the blue component. Column (11): radial velocity shift of the line peak in km s $^{-1}$.

Table 4. Spectrophotometric Quantities of the [OIII] components of this work.

Jcode	[OIII] NC			[OIII] Blue			
	F	W	FWHM	F	W	FWHM	shift
(1)	(2)	(3)	(4)	(5)	(6)	(7)	(8)
J084502	521 \pm 20	3 \pm 0.1	500 \pm 43	2581 \pm 998	12 \pm 1	3012 \pm 263	-2257 \pm 379
J093403	-	-	-	-	-	-	-
J105427	-	-	-	-	-	-	-
J125914	1517 \pm 64	9 \pm 0.4	1084 \pm 102	-	-	-	-
J144218	140 \pm 11	3 \pm 0.2	1515 \pm 50	-	-	-	-
J210831	650 \pm 35	3 \pm 0.2	905 \pm 104	750 \pm 42	3 \pm 0.2	1513 \pm 179	-2215 \pm 433

Notes: All measurements are in the quasar rest-frame, and line fluxes are all in units of 10^{-17} erg s $^{-1}$ cm $^{-2}$. Uncertainties are computed using the quality parameter Q defined by Marziani et al. (2022). Column (1): SDSS identification of the object. Column (2): total flux of [OIII] NC. Column (4): equivalent width of [OIII] NC, in Å. Column (5): FWHM [OIII] NC, in km s $^{-1}$. Columns (8) to (10): same as [OIII] NC but for the blue component (if detected). Column (8): radial velocity shift of the line peak in km s $^{-1}$.

found that contaminated the blue wing of the doublet profile, and they were incorporated into the `specfit` model. The sources did not exhibit a blue component except for J0845 and J1054 (FWHM \approx 5300 km s $^{-1}$), which had low intensity and were asymmetrical (especially in the latter case), probably due to the detect absorption.

5.1.5 H β

This was the LBT sample consisting of good S/N spectra (\sim 10-20, except for the case of J1442 which had a value of \approx 4). A precise separation of the BC and Blue components could be achieved, not only for H β but also for [OIII] (which, as previously mentioned, is a HIL that also shows outflows), as in the J2108 case. On the other hand, due to the high contribution of FeII, it was impossible to detect the [OIII] emission, for instance in J0934 and J1054. The case of J1259 is particularly noteworthy, as it has FWHM \approx 2000 km s $^{-1}$, which is almost at the limit of an NLSy1-type quasars (Osterbrock & Pogge 1985). The narrowness of the lines is peculiar due to the source high luminosity (Marziani et al. 2018b).

5.1.6 [OIII] $\lambda\lambda$ 4959,5007

[OIII] emission is expected to be weak in this type of object, where FeII emission is very prominent and accretion is high (Boroson & Green 1992; Sulentic et al. 2000; Marziani et al. 2016; Vietri et al. 2018; Temple et al. 2024; Deconto-Machado et al. 2024). In J0934 and J1054 in fact, no [OIII] emission is detected at all. In J1442 the detection is weak, being lost in the noise. On the other hand, in J0845, J1259 and J2108 a narrow [OIII] component is observed

which, although not very prominent, confirms the rest-frame of the object based on the peak of H β and AlIII λ 1860. Only in J0845 a semi broad component of [OIII] shifted to blue is detected. In J2108, we have also included a blueshifted [OIII] component, although in this object it is weak and with a similar width to the [OIII] component in the rest-frame. The fluxes of the [OIII] components are reported in Table 4.

5.2 Emission line profiles in the xA quasars

In Table 6 we report, for each object, the parameters associated with the full profile measurements of CIV, MgII, SiIV, AlIII, and H β . These parameters are the FWHM, the asymmetry index (AI) and the centroids of each emission line. The centroid at fraction x of the peak intensity is given by:

$$c(x) = \frac{\lambda_{R(x)} + \lambda_{B(x)} - 2\lambda_0}{2\lambda_0} c, \quad (1)$$

where $\lambda_{R(x)}$ and $\lambda_{B(x)}$ are the wavelengths in the red (R) and blue (B) wings, respectively. Values reported are for $x = 0.25, 0.5, 0.75$, and 0.9.

Table 5. Spectrophotometric Quantities of the UV regions of this work.

Jcode	Stiv				Oiv]		Siv Blue			
	$F_{\lambda}(1350\text{\AA})$	F	W	FWHM	F	FWHM	F	W	FWHM	shift
(1)	(2)	(3)	(4)	(5)	(6)	(7)	(8)	(9)	(10)	(11)
J084502	631±16	1514±106	2±0.1	1587±159	1892±113	3±0.1	6368±382	10±0.6	10036±803	-1777±404
J093403	1390±29	-	-	-	-	-	-	-	-	-
J105427	881±23	-	-	-	-	-	-	-	-	-
J125914	1365±15	4003±200	3±0.1	1650±116	4003±280	3±0.1	4980±249	4±0.2	10008±801	-1489±255
J144218	322±11	1024±61	3±0.1	2626±236	1024±61	3±0.1	1754±88	5±0.2	10003±700	-1604±795
J210831	2211±50	2038±143	1±0.1	3830±421	2547±127	1±0.1	10546±527	5±0.2	9983±699	-1498±330

Jcode	Civ				HeII		CivBlue				HeI Blue			
	F	W	FWHM	F	W	FWHM	F	W	FWHM	shift	F	W	FWHM	shift
(1)	(2)	(3)	(4)	(5)	(6)	(7)	(8)	(9)	(10)	(11)	(12)	(13)	(14)	(15)
J084502	7023±421	10±0.4	5664±510	1558±78	2±0.1	5234±366	7008±420	13±0.5	10388±935	-2233±373	1447±72	3±0.1	4893±489	-1726±201
J093403	9382±563	6±0.2	4352±392	5904±295	5±0.1	6037±483	695±28	0.5±0.05	5034±252	-4527±103	1814±91	1±0.1	5087±458	-1648±254
J105427	3084±111	2±0.1	4613±318	705±28	0.7±0.05	4299±258	3308±165	4±0.2	10639±745	-3214±450	1533±61	2±0.1	5049±505	-1855±217
J125914	7154±572	5±0.2	2534±304	1849±92	1±0.1	4195±336	8035±482	6±0.2	10561±950	-918±846	1775±89	1±0.1	4980±598	-1881±129
J144218	1907±114	6±0.2	3728±298	596±30	2±0.1	4468±268	2985±149	9±0.2	10550±844	-2980±763	647±26	2±0.1	6633±597	-3032±237
J210831	5313±266	2±0.1	5590±391	1327±53	0.5±0.05	4489±269	16690±835	7±0.2	10812±865	-4424±509	1270±51	0.6±0.05	4850±728	-1474±81

Jcode	AlII				SiIII]		CIII]		FeII			
	$F_{\lambda}(1700\text{\AA})$	F	W	FWHM	F	FWHM	F	FWHM	F	W	FWHM	shift
(1)	(2)	(3)	(4)	(5)	(6)	(7)	(8)	(9)	(10)	(11)	(12)	(14)
J084502	516±12	3573±965	7±2	4536±253	3940±1379	4069±651	1988±119	3962±634	19±1	773±62	2±0.5	4893±489
J093403	1178±36	4452±1024	4±1	4073±484	5597±336	3501±560	5287±317	3272±523	45±2	1768±248	2±0.5	5087±458
J105427	710±14	3287±788	4±1	4552±360	3019±181	4110±658	718±7	3498±525	28±1	1065±107	2±0.5	5049±505
J125914	941±18	2589±595	4±1	2478±167	2826±113	1994±319	3341±100	1776±284	30±2	-	-	-
J144218	234±17	1518±228	6±2	3743±345	1274±115	3395±509	587±65	3156±473	9±1	100±1	0.4±0.05	4980±598
J210831	1568±27	9878±2074	6±2	5534±805	10976±440	5300±848	1333±147	4850±728	47±2	1720±206	1±0.1	6633±597

Jcode	MgII				FeII		MgII Blue			
	$F_{\lambda}(3000\text{\AA})$	F	W	FWHM	F	FWHM	F	W	FWHM	shift
(1)	(2)	(3)	(4)	(5)	(6)	(7)	(8)	(9)	(10)	(11)
J084502	270±81	8592±430	30±2	3849±308	107±9	669±24	2±0.1	5384±185	-1474±81	-
J093403	949±49	17290±1141	17±1	3463±346	443±44	-	-	-	-	-
J105427	352±78	8813±441	24±1	3769±302	169±14	434±14	1±0.05	5313±213	-1499±76	-
J125914	460±106	8487±509	18±1	1416±127	230±18	-	-	-	-	-
J144218	101±57	1508±75	26±1	3000±210	56±4	-	-	-	-	-
J210831	-	-	-	-	-	-	-	-	-	-

Notes: All measurements are in the quasar rest-frame, and line fluxes are all in units of 10^{-17} erg s^{-1} cm^{-1} . **Top:** SDSS identification of the object. Column (1): continuum flux at 1350Å. Columns (3,6,8): total flux. Column (4,7,9): equivalent width in Å. Column (5,10): FWHM in km s^{-1} . Column (11): radial velocity shift of the line peak. **Middle top:** Column (1): SDSS identification of the object. Columns (2,5,8,12): total flux. Column (3,6,9,13): equivalent width in Å. Column (4,7,10): FWHM in km s^{-1} . Column (11,14): radial velocity shift of the line peak. **Middle bottom:** Column (1): SDSS identification of the object. Columns (2,6,10,11): total flux. Column (4,12): equivalent width in Å. Column (5,7,9,13): FWHM in km s^{-1} . Column (14): radial velocity shift of the line peak. **Bottom:** Column (1): SDSS identification of the object. Columns (2,3,6,7): total flux. Column (4,8): equivalent width in Å. Column (5,9): FWHM in km s^{-1} . Column (10): radial velocity shift of the line peak in km s^{-1} .

The asymmetry index is different from zero (negative) only for objects with a blueshifted component. The asymmetry index at one quarter is defined as line displacement with respect to the peak wavelength (in practice the $c(0.9)$ is used as a proxy for λ_P) normalized by line width at $\frac{1}{4}$ intensity,

$$AI = \frac{\lambda_{R(\frac{1}{4})} + \lambda_{B(\frac{1}{4})} - 2\lambda_P}{\lambda_{R(\frac{1}{4})} - \lambda_{B(\frac{1}{4})}} \quad (2)$$

These parameters are measured on the full profiles, and therefore avoid the uncertainties associated with the decomposition of the line profiles. On the full profiles of $H\beta$, $AlIII$, $MgII$, it is necessary to compute the centroid at a low fractional intensity (i.e., $\frac{1}{4}$) to detect the effect of the BLUE component (Table 6).

The full profile analysis confirms the result of the multi-component decomposition: the observed $CIV\lambda1549$ and $SIV\lambda1397$ blueshifts spreads up to -4000 , with value increasing toward low fractional intensity. As for the ratio R_{FeII} , sources with a higher ratio, $CIV\lambda1549$ and $SIV\lambda1397$ centroids tends to be highly blueshifted. Whereas in $H\beta$, $AlIII$ and $MgII$ there is no strong dependence on line luminosity, R_{FeII} , and FWHM; data points are around zero radial velocity i.e., consistent with the rest frame of the quasar.

Overall, it seems that there is no systematic blueshift towards highest Eddington ratios, nor with luminosity. This is hardly surprising because the sources are only 5, at similar luminosity. The spread in Eddington ratio is also modest with all sources having $L/L_{Edd}(H\beta) \gtrsim 0.6$. J1259 is an outlier with $L/L_{Edd} \gtrsim 2$ in all estimates, due to its very narrow lines.

It is interesting to note, however, that the shift amplitude tends to increase with ionization potential of the parent ionic species: from $H\beta$ and $MgII\lambda2800$ with $\chi \sim 10$ eV showing modest shifts even toward the line base, we reach a maximum shift ~ -5000 km s $^{-1}$ for $CIV\lambda1549$, with $\chi \sim 60$ eV. Fig. 4 confirms that this trend is present in most of the sample sources. Additionally, we observe a systematic increase in the line width when comparing $H\beta$ and $CIV\lambda1549$: the FWHM ratio with respect to $H\beta$ is approximately 2. The high shift amplitude and larger FWHM indicate a spectroscopically resolved component affecting the high-ionization line profiles. In other words, the excess broadening in $CIV\lambda1549$ is due to the prominence of its blueshifted component, which remains fainter in $H\beta$ (implying $CIV\lambda1549/H\beta \gg 1$). In other words, the increase in FWHM from low to high ionization lines is not mainly due to a decrease in emissivity-weighted distance (which would be expected in case of a Keplerian velocity field), but to the onset of an addition component displaced in radial velocity (Sulentic et al. 2007; Marziani et al. 2016). The only exception in this respect appears J0934: it is a BAL, and we cannot exclude that part or all of the blueshifted emission is removed by the broad absorption.

5.3 Consistency of criteria to identify super-Eddington candidates

The location of the six sources, both in the optical and UV planes, defined by FWHM ($H\beta$) vs. R_{FeII} , and the intensity ratios $CIII\lambda1909/SiIII\lambda1892$ vs. $AlIII\lambda1860/SiIII\lambda1892$, respectively, is shown in Figure 5. According to Sulentic et al. (2000), the xA quasars that meet the criteria $R_{FeII} > 1.0$ (red dashed line) are a sub-population of Population A. Following MS14, the extreme quasars (green shaded area) also meet the criteria: $AlIII/SiIII > 0.5$ & $SiIII/CIII > 1$ (enclosed in grey dashed lines). The yellow upside-down triangles are the luminosity-dependent limit between

Pop. A and Pop. B. of Sulentic et al. (2017, gold), which brings the limit at $FWHM \approx 4000$ km s $^{-1}$ to significantly higher values for sources of bolometric luminosity $\log L_{bol} \gtrsim 46$ ergs s $^{-1}$: $FWHM_{AB} \approx 3500 + 500(L_{bol}/3.69 \times 10^{44})^{0.15}$ km s $^{-1}$ (applied to $H\beta$). Each source is uniquely identified, enabling visualization of the object-position in the optical plane. Note that, if the FWHM $H\beta$ is cleaned of the excess emission due to the BLUE nonvirial component, all sources meet the line width criterion for being of Population A as seen in Fig. 5 (black dots, left).

Of the six sources of the present sample, five meet both the UV and optical criteria (J1259 is consistently not an xA, since $R_{FeII} \ll 1$ and $CIII\lambda1909/SiIII\lambda1892$ vs. $AlIII\lambda1860/SiIII\lambda1892$ are too high and too low, respectively). The discordant source is J0845 which falls in the xA UV rectangle, albeit of spectral type A2 ($R_{FeII} \approx 0.7-0.8$). To improve the statistics, in addition to the six sources of the LBT sample (stars), we added in Fig. 5 (right), sources identified as Pop. A3 (circles) and Pop. A4 (squares) by Marziani et al. (2022); Deconto-Machado et al. (2023, 2024). We also included five quasars from the MS14 UV sample (black contours), which were observed in Matthews et al. (2021) and Temple et al. (2024). Fig. 5 (right) shows that out of 28 sources confirmed as xA quasars (Pop. A3-A4) using the optical selection criterion $R_{FeII} \gtrsim 1$, between three (if we exclude borderline cases) and seven do not meet the UV line ratios selection criteria, implying that between $\sim 75\%$ and 90% of optically-classified A3-A4 quasars fall within the UV xA region.

The lack of a one-to-one correspondence may due to inaccuracies in the fitting of the $CIII\lambda1909$ emission line, especially because of contamination from $FeIII\lambda1914$ emission in its red wing, which may not have been properly taken into account. The epoch difference between optical and UV observations could also introduce inconsistencies. The spectra obtained with LUCI are separated by several years from those acquired by the SDSS, leaving open the possibility of considerable variation (Punsly et al. 2016). The MJD of the SDSS spectra ranges from 52,000 to 58,000, whereas most LBT observations are around 57,000. Variability is unlikely to significantly affect the classification: although emission lines do respond to continuum changes, a variation in their ratios would require a change in the physical conditions of the emitting gas — a scenario that appears improbable.

The expectation is that both selection criteria will help us identify the highest accreting quasars (super-Eddington candidates) for cosmological purposes, which will be discussed in Sect. 6.4. The statistics is still limited, but our preliminary analysis suggests that the two criteria might be consistently met in about 80% of cases.

5.4 General considerations

The $H\beta$ blueshifted emission is detectable on $H\beta$ in three sources (J084502, J093403, and J210831). The $H\beta$ BLUE component is most likely associated with an outflow which produces the prominent blueshifted emission more clearly observed in $CIV\lambda1549$ profiles (e.g., Coatman et al. 2016; Sulentic et al. 2017). In contrast, the CIV blueshifted emission is clearly detectable in all sources (except in J093403 where it seems that the emission is severely contaminated by an absorption), implying that the intensity ratio $CIV/H\beta$ can be expected to be $\gg 1$.

The picture emerging from the previous analysis emphasizes the difference between the xA candidates and the Population A and B AGN at both low and high luminosity. Five of the six sources of the present sample show properties that make them similar to other xA sources observed at low- and high-luminosity: strong $FeII$, weak $[OIII]$, blue-shifted $CIV\lambda1549$ and almost symmetric $H\beta$ (Marziani

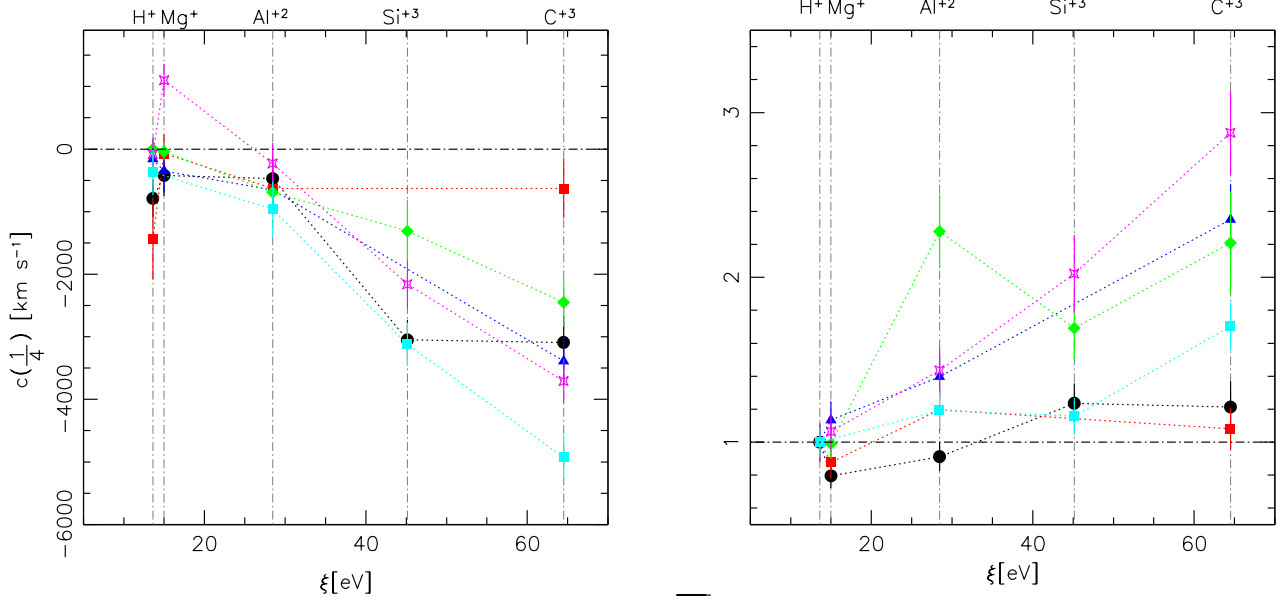


Figure 4. Shift amplitude of the centroid at $\frac{1}{4}$ peak intensity (left) and FWHM / FWHM ($H\beta$) ratios vs. ionization potential χ (right) for the ionic species associated with the emission lines considered in this study. Different colors and symbols identify different object in the sample. Black circles: J0845; red squares: J0934; blue triangles: J1054; green rhombuses: J1259; magenta stars: J1442; cyan squares: J2108.

Table 6. Line profile parameters

Jcode	Line	FWHM	AI	$c(\frac{1}{4})$	$c(\frac{1}{2})$	$c(\frac{3}{4})$	$c(0.9)$
J084502	CIV	7000 ± 750	-0.12 ± 0.07	-3090 ± 420	-3050 ± 380	-2790 ± 230	-2340 ± 120
J084502	MgII	4590 ± 300	-0.03 ± 0.09	-420 ± 330	-340 ± 150	-290 ± 110	-290 ± 80
J084502	SiIV	7130 ± 480	-0.53 ± 0.07	-3050 ± 310	-2110 ± 240	-1130 ± 340	-340 ± 160
J084502	AlIII	5260 ± 330	-0.03 ± 0.08	-470 ± 320	-450 ± 160	-370 ± 140	-340 ± 90
J084502	Hβ	5770 ± 390	-0.16 ± 0.07	-790 ± 300	-820 ± 190	-240 ± 180	-110 ± 80
J093403	CIV	4580 ± 360	-0.14 ± 0.11	-630 ± 470	-130 ± 180	-50 ± 120	-30 ± 80
J093403	MgII	3720 ± 250	0.00 ± 0.09	-70 ± 300	-70 ± 130	-80 ± 100	-80 ± 60
J093403	AlIII	5070 ± 310	-0.06 ± 0.07	-630 ± 280	-550 ± 160	-440 ± 140	-400 ± 90
J093403	Hβ	4240 ± 350	-0.29 ± 0.14	-1430 ± 650	-130 ± 170	-40 ± 120	-20 ± 70
J105427	CIV	9120 ± 510	-0.30 ± 0.06	-3390 ± 380	-2780 ± 260	-2000 ± 290	-1410 ± 190
J105427	MgII	4400 ± 290	-0.07 ± 0.09	-350 ± 330	-270 ± 150	-230 ± 180	-80 ± 70
J105427	AlIII	5420 ± 330	-0.04 ± 0.07	-650 ± 300	-610 ± 160	-510 ± 150	-460 ± 100
J105427	Hβ	3880 ± 280	-0.04 ± 0.09	-160 ± 290	-90 ± 140	-50 ± 110	-30 ± 70
J125914	CIV	4440 ± 540	-0.43 ± 0.10	-2450 ± 380	-1390 ± 270	-750 ± 140	-670 ± 60
J125914	MgII	1990 ± 110	0.03 ± 0.08	-40 ± 130	-40 ± 50	-60 ± 50	-80 ± 40
J125914	SiIV	3400 ± 310	-0.43 ± 0.14	-1310 ± 490	50 ± 150	300 ± 70	280 ± 110
J125914	AlIII	4580 ± 310	-0.30 ± 0.06	-690 ± 210	-420 ± 160	90 ± 180	350 ± 70
J125914	Hβ	2010 ± 140	0.00 ± 0.10	0 ± 170	10 ± 70	10 ± 60	10 ± 30
J144218	CIV	8920 ± 460	-0.30 ± 0.06	-3710 ± 350	-3080 ± 230	-2370 ± 250	-1850 ± 160
J144218	MgII	3300 ± 220	0.01 ± 0.09	1100 ± 260	1100 ± 110	1090 ± 90	1090 ± 60
J144218	SiIV	6270 ± 570	-0.39 ± 0.08	-2160 ± 370	-1190 ± 280	-370 ± 170	-200 ± 110
J144218	AlIII	4450 ± 290	-0.03 ± 0.09	-230 ± 320	-160 ± 140	-130 ± 120	-140 ± 80
J144218	Hβ	3100 ± 220	-0.03 ± 0.10	-80 ± 260	-30 ± 110	-10 ± 80	0 ± 50
J210831	CIV	9860 ± 520	-0.07 ± 0.05	-4930 ± 360	-4660 ± 260	-4580 ± 280	-4430 ± 190
J210831	SiIV	6700 ± 450	-0.29 ± 0.07	-3120 ± 340	-2660 ± 230	-2080 ± 230	-1640 ± 140
J210831	AlIII	6910 ± 460	-0.08 ± 0.08	-960 ± 430	-850 ± 230	-640 ± 190	-540 ± 120
J210831	Hβ	5790 ± 380	-0.04 ± 0.08	-370 ± 360	-330 ± 190	-240 ± 160	-190 ± 100

Notes: All measurements are in the quasar rest frame; centroids and FWHM are in km s^{-1} .

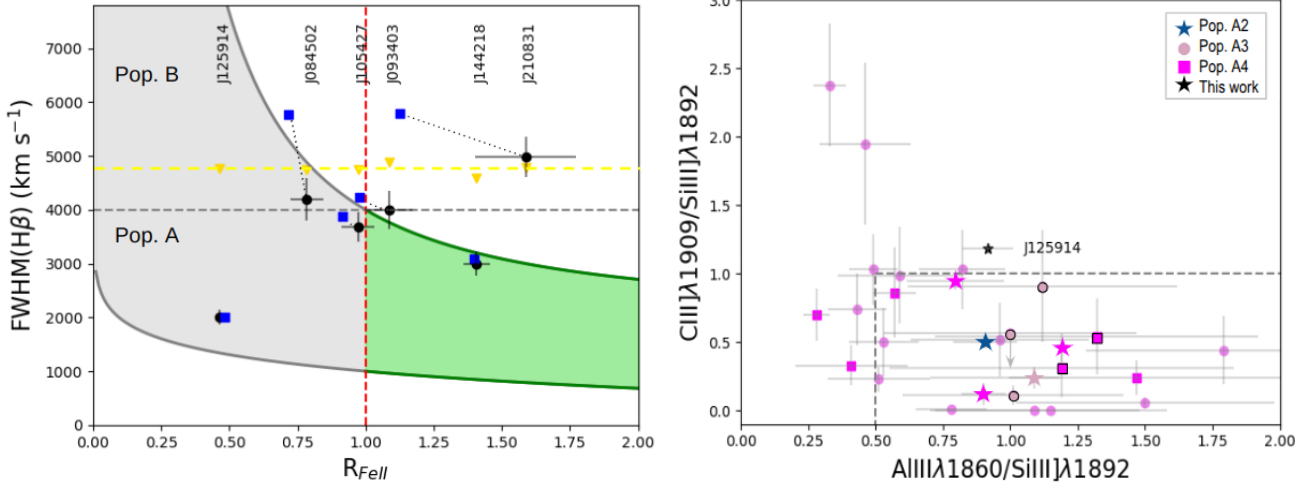


Figure 5. Distribution of the LBT sample in the optical (left) and UV (right) plane. *Left:* The luminosity-dependent limit between Pop. A and Pop. B. of Sulentic et al. (2017) is shown in gold. The blue squares show the position within the sequence using only the BC for the $H\beta$ FWHM, while black circles make use of the full profile (i.e. BC+Blue) are in blue. The shaded area is a schematic representation of the Main Sequence of quasars for low- z samples. *Right:* Pop. A3 (circle) and A4 (square) quasars shown in the UV plane are from Marziani et al. (2022); Deconto-Machado et al. (2023, 2024). The magenta and purple colors identify spectral type A3 and A4, respectively. Data outlined with a black contour represent quasars from Marziani & Sulentic (2014). Their rest-frame optical spectra were obtained from Matthews et al. (2021) and Temple et al. (2024).

et al. 2014; Marziani & Sulentic 2014; Negrete et al. 2018; Martínez-Aldama et al. 2018; Deconto-Machado et al. 2023, 2024). The properties are consistent with the one found at the high R_{FeII} tip of the quasar main sequence (Boroson & Green 1992; Sulentic et al. 2000; Marziani et al. 2018a). In this respect, it is remarkable that 3 sources out of 5 have been detected in the radio. At redshift $\lesssim 1$, quasars of spectral types A3 and A4 often show significant radio emission, placing them in the radio-detected and intermediate domain (Ganci et al. 2019, $10 \lesssim R_K \lesssim 80$ according to Zamfir et al. 2008). This radio emission has been ascribed to star formation processes because of its correlation with FIR parameters (Sani et al. 2010; Bonzini et al. 2015; Caccianiga et al. 2015; Netzer et al. 2016; Marziani et al. 2021).

Only, at high luminosity, lines are broader (because of the higher black hole masses, Marziani et al. 2018b) and blueshifts reach the highest amplitudes (~ -5000 km s $^{-1}$) because of the stronger radiation force and of the high L/L_{Edd} (Sulentic et al. 2017). Blueshifts appear ubiquitous and dominating in the high-ionization line profiles (see Fig. 2 and Fig. 3), suggesting dominance of outflows, and likely radiative acceleration. At the same time, the $H\beta$ profile remains fairly symmetric and unshifted, suggesting the presence of a virialized component even at the highest luminosity (Marziani & Sulentic 2014; Sulentic et al. 2007; Gillette & Hamann 2024). These results are consistent with other recent analyses, also for [OIII] (Fiore et al. 2017; Bischetti et al. 2017; Vietri et al. 2018; Kakkad et al. 2020).

6 DISCUSSION

In this section, we will discuss the estimation of physical parameters such as black hole mass and Eddington ratio, along with considerations and estimations regarding the winds/outflows of C1vλ1549 and [OIII]. Additionally, we will build a Hubble diagram using the highly accreting quasar sample from the LBT within the cosmological context.

6.1 L_{bol} , M_{BH} and Eddington ratio

The bolometric correction (B.C.) for 1700, 3000 and 5100Å were computed using $B.C. = c \times [L/(10^{42} \text{ ergs s}^{-1})]^d$ and the constants of Table 1 by Netzer (2019), and the values of Richards et al. (2006) modified by the redshift. L/L_{Edd} and L_{bol} values for the three lines are reported in Table 7, using the specified B.C. and the appropriate scaling relations (Marziani et al. 2022; Trakhtenbrot & Netzer 2012; Vestergaard & Peterson 2006). The Eddington luminosity was computed for the masses obtained from the FWHM of AlIII, MgII, and $H\beta$ emission lines following the relation: $L_{Edd} \approx 1.5 \times 10^{38} (M_{BH}/M_{\odot})$ [ergs s $^{-1}$] (e.g. Netzer & Marziani 2010; Netzer 2015).

Using the FWHM of the MgIIλ2800 line, we computed the virial M_{BH} using Eq. 3:

$$\log \left(\frac{M_{BH, \text{vir}}}{M_{\odot}} \right) = a + b \log \left(\frac{L}{10^{44} \text{ erg/s}} \right) + c \log \left(\frac{\text{FWHM}}{\text{km/s}} \right), \quad (3)$$

and the a , b , c values from Table 5 of Shen & Liu (2012)² Using the FWHM of AlIIIλ1860, we applied the scaling law of M22 to compute the $M_{BH}(\text{AlIII})$. Using the FWHM of $H\beta$, we considered Eq. 7 of Floris et al. (2024), which is specifically tailored for high-accretion rate sources. The $M_{BH}(H\beta)$ formula is based on the Vestergaard & Peterson (2006) relation with two key modifications: (1) a correction to the FWHM as proposed by Mejía-Restrepo et al. (2018), and (2) the inclusion of the dependence of the BLR radius on R_{FeII} as described by Du & Wang (2019). Table 7 reports the M_{BH} estimates for the three lines.

The behavior of the M_{BH} values is shown in Fig. 6 with respect to $H\beta$. In the abscissa scale is $\log M_{BH}(H\beta)$ (using Shen & Liu 2012) vs. $\log M_{BH}$ of AlIII and MgII (using Marziani et al. 2022 for the former, and Shen & Liu 2012 for the latter). The Pearson correlation for each estimation is 0.89 for AlIII while for MgII is 0.96. The values of these correlation coefficients show a very good agreement between

² This was done in order to minimize the difference in virial mass calibrations, using the one by Vestergaard & Peterson (2006) as standard.

Table 7. Accretion parameters.

Jcode	AlIII					
	log L_{bol}		log M_{BH}		L/L_{Edd}	
	BC N19	a N19	M22	N19		
(1)	(2)	(3)	(4)	(5)	(6)	
J084502	3.11	47.25	47.11	9.34	0.63	
J093403	2.90	47.56	47.39	9.43	1.06	
J105427	3.04	47.34	47.19	9.40	0.69	
J125914	2.97	47.45	47.29	8.93	2.59	
J144218	3.38	46.88	46.78	8.96	0.65	
J210831	2.78	47.73	47.54	9.79	0.68	

Jcode	MgII					
	log L_{bol}		log M_{BH}		L/L_{Edd}	
	BC N19	b N19	TN12	SL12	b N19	N19
(1)	(7)	(8)	(9)	(10)	(11)	(12) (13)
J084502	3.03	47.29	47.06	9.52	9.30	0.77 0.46
J093403	2.41	47.79	47.46	9.73	9.45	1.70 0.80
J105427	2.94	47.36	47.12	9.54	9.30	0.9 0.52
J125914	2.80	47.47	47.20	8.76	8.70	4.57 2.48
J144218	3.73	46.84	46.70	9.02	8.63	1.28 0.93
J210831	-	-	-	-	-	-

Jcode	H β							
	log L_{bol}			log M_{BH}		L/L_{Edd}		
	BC N19	c N19	VP06	SL12	F24	c N19		
(1)	(14)	(15)	(16)	(17)	(18)	(19)	(20)	(21)
J084502	4.79	47.57	47.19	9.40	9.36	9.44	1.28	0.59
J093403	3.67	48.15	47.51	9.56	9.54	9.63	3.25	0.97
J105427	4.95	47.50	47.23	9.31	9.17	9.33	1.67	0.9
J125914	4.94	47.51	47.53	8.78	8.64	9.22	5.72	3.05
J144218	6.27	46.99	46.82	8.88	8.78	8.96	1.27	0.86
J210831	4.71	47.61	47.32	9.63	9.40	9.41	1.29	0.65

Notes: Columns: (1) SDSS identification. (2,7,14) Bolometric correction (BC) computations following [Netzer \(2019\)](#). (3,8,15) and (4,9,16), Log of Bolometric luminosity in units of erg s^{-1} using [Richards et al.](#) ($a=4.3$, $b=5.15$, and $c=9.26$, 2006), and BC from [Netzer \(2019\)](#), respectively. Uncertainty is 10% the luminosity. (5,10,11,17,18) Black hole mass in unit of M_{\odot} . Below each column is detailed which scalar relation is used: [Marziani et al. \(2022\)](#) is M22, [Trakhtenbrot & Netzer \(2012\)](#) is TN12, [Vestergaard & Peterson \(2006\)](#) is VP06, [Shen & Liu \(2012\)](#) is SL12, and [Floris et al. \(2024\)](#) is F24. (6,12,13,20,21). Eddington ratio with different BC factors using [Netzer \(2019\)](#) or [Richards et al. \(2006\)](#).

the M_{BH} estimates employing different lines. The solid lines are the best fits obtained using the least-square method: $\log M_{\text{BH}}(\text{MgII}) \approx 0.97 \log M_{\text{BH}}(\text{H}\beta) + 0.25$ and $\log M_{\text{BH}}(\text{AlIII}) \approx 0.75 \log M_{\text{BH}}(\text{H}\beta) + 2.38$. As for the $\text{H}\beta$ M_{BH} estimations, [Floris et al. \(2024\)](#) and [Shen & Liu \(2012\)](#), the values reported in Table 7 (Cols. 17-19), the values from [Floris et al. \(2024\)](#) show a very good agreement with the estimates from [Vestergaard & Peterson \(2006\)](#), with average $\delta \log M_{\text{BH}} \approx 0.07 \pm 0.21$, and a slight systematic difference with [Shen & Liu \(2012\)](#): $\delta \log M_{\text{BH}} \approx 0.18 \pm 0.20$. The scatter might be associated with the correction for orientation (included in F24, but not in SL12 and VP06): the largest $\delta \log M_{\text{BH}} \approx 0.5$ occurs right for J125914, the object with the narrowest $\text{H}\beta$ line in the sample. The small systematic effect between SL12 and [Floris et al. \(2024\)](#) is less clear, but the amplitude of the offset, about 50%, is well within the systematic uncertainty of the scaling laws based on $\text{H}\beta$ ([Marziani & Sulentic 2012](#); [Shen 2013](#)).

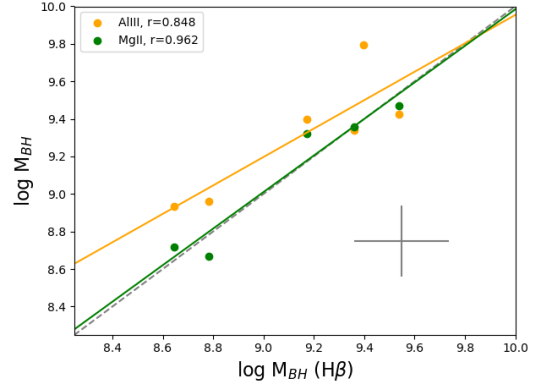


Figure 6. Distribution of $\log M_{\text{BH}}$ of $\text{H}\beta$ (abscissa) vs. $\log M_{\text{BH}}$ of AlIII and MgII (ordinate), with the Pearson correlation of each computation. Dashed line is the equity line. Error bar are the mean values of the AlIII and MgII uncertainties: 0.26 and 0.32, respectively.

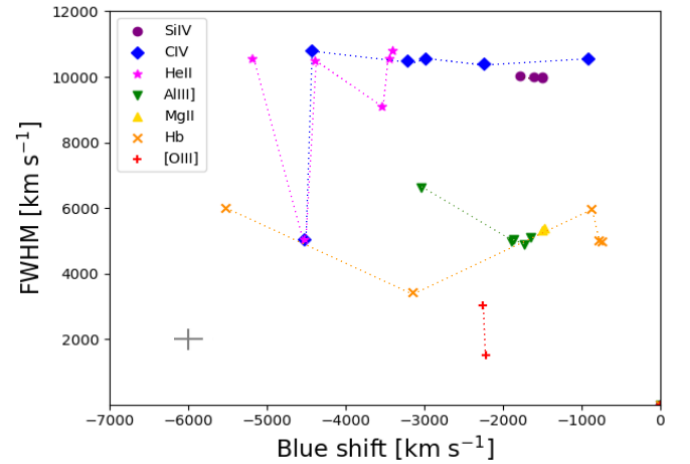


Figure 7. Distribution of shifts of the Blue component (if detected) on the profile lines of CIV, SiIV, HeII, AlIII, MgII, $\text{H}\beta$, and [OIII] (in the case of [OIII] is the semi-broad component blueshifted). Error bar are the mean values of the uncertainties of the FWHM and blueshifts: 310 and 250 km s^{-1} , respectively.

6.2 Wind models

Line profiles associated to xA quasars such as the ones of the LBT sample (as seen in Figs. 2 and 3, with a presence of a BC and additional one) can be tentatively modeled with a radial flow, possibly due to a radiation-driven wind (e.g. [Zamanov et al. 2002](#); [Risaliti & Elvis 2010](#)). Alternative models involve magnetically driven centrifugal acceleration ([Emmering et al. 1992](#)). Both wind acceleration mechanisms are favored at high luminosity and mass ([Proga 2007](#)), and it is still not fully known which one is actually operating ([Elitzur et al. 2014](#)), if they are concomitant, or applicable to different sources. The CIV λ 1549 line shift with respect to RF offers a fundamental test of disk wind models: winds driven by radiation pressure do not conserve the angular momentum of the gas flow and produce a mostly radial outflow ([Elvis 2000](#)) with very large blueshifts. Magnetically-driven acceleration produces more symmetric, less shifted profiles. The large shift amplitudes observed in the LBT sample ($\gtrsim 2000 \text{ km s}^{-1}$) favor the radiation-driven hypothesis.

The blueshift interpretation involves emitting gas motion towards the observer causing Doppler shift of line radiation ([Marziani et al.](#)

2017). The distribution of the blueshifts (if detected) for the emission lines: C IV, Si IV, He II, Al III, Mg II, H β , and [O III] is shown in Fig. 7. The UV lines (C IV and Si IV) shows larger shifts; on the converse, Al III, H β , and Mg II present moderate shifts as indicated in Martínez-Aldama et al. (2018); Buendia-Rios et al. (2023). The semi-broad component of [O III] was only detected in two sources and showed a shift of $\sim 2000 \text{ km s}^{-1}$. Error bar represents the mean values of the uncertainties of the FWHM and blueshifts: 310 and 250 km s^{-1} , respectively. Although the [O III] shift is large, we will restrict most of the following analysis to the line that is apparently most affected by the outflow, namely C IV $\lambda 1549$.

Outflow parameters determination

Several caveats and assumptions accompany the computation of the kinetic power and thrust from single-epoch spectra. In AGN outflows, the thrust is the force exerted by winds in the innermost regions. The outflows can be propelled by several mechanisms such as radiation pressure, magnetic fields, and accretion disk winds. They can exert significant thrust on the surrounding interstellar medium (ISM) or intracluster medium (ICM). The "thrust" of the wind generally refers to the force exerted by the wind itself. The kinetic power refers to the rate at which kinetic energy is transported away and can be computed knowing the outflow mass flux and the outflow velocity. The kinetic power and thrust provides insights into the impact of outflows on their surrounding environments and in driving material away from the central black hole, regulating star formation and influence the gas content of the host galaxy (Liu et al. 2013a,b).

Here, we follow the method for estimating the mass of ionized gas (M^{ion}), the mass outflow rate (\dot{M}^{ion}), the thrust ($\dot{M}^{\text{ion}} k v_0$), and the kinetic power ($\dot{\epsilon}$) of the outflow for collisionally excited lines in photoionized gases (Cano-Díaz et al. 2012) by Marziani et al. (2017, hereafter M17). M17 devised a framework that enables deriving outflow parameters independently from the covering and filling factors, assuming uniform gas density across all emitting regions. The following specific assumptions are necessary to apply the following relation to measurements of C IV obtained from single epoch spectra:

- constant electron density, $n \text{ [cm}^{-3}\text{]}$;
- all gas being in the same ionization stage;
- well-defined chemical abundances, $Z \text{ [Z}_\odot\text{]}$;
- typical emitting radius, $r \text{ [r}_g\text{]}$;
- outflow velocity, $v_o \text{ [km s}^{-1}\text{]}$.

This simplified approach is suitable for elucidating the influence of outflow parameters on thrust and kinetic power calculations with the equations of M17.

It should be noted that the outflow estimations derived from the Blue components of C IV $\lambda 1549$ using the equations proposed by M17 assumed a spectral energy distribution (SED) for low-redshift and low-bolometric luminosity quasars. Given that the LBT sample are high-redshift ($z \sim 2$) and high-luminosity sources, the softening of the accretion disk emission due to larger M_{BH} makes the SED significantly different than the one of low- L (Duras et al. 2017, 2020), reducing the amount of ionizing photons. We therefore consider the re-computation of the conversion between line luminosity of C IV $\lambda 1549$ and amount of gas by Deconto-Machado et al. (2024).

Deconto-Machado et al. (2024) considered observational constraints to estimate the outflow parameters from the C IV emission line: (a) the C IV equivalent width of is typically very low $W \sim 10 \text{ \AA}$ and in Pop. A $W \leq 30 \text{ \AA}$ (Martínez-Aldama et al. 2018), and (b) the C IV $\lambda 1549/\text{H}\beta$ ratio can be assumed to be $\text{C IV}/\text{H}\beta \geq 5 \sim 10$, due to

the absence of a strong H β blueshifted component. These conditions are encountered for the LBT sample: $W(\text{C IV}) \approx 4 - 13$. Deconto-Machado et al. performed CLOUDY computations that uses a SED appropriate for high L , from Krawczyk et al. (2013), which yields estimates in agreement with those of Vietri et al. (2020). For the sake of clarity, we report below the expressions used for C IV $\lambda 1549$.

$$M^{\text{ion}} \sim 5 \cdot 10^2 L_{45} \left(\frac{Z}{Z_\odot} \right)^{-1} n_9^{-1} M_\odot$$

$$\dot{M}^{\text{ion}} \sim 8 L_{45} v_{o,5000} r_{1\text{pc}}^{-1} \left(\frac{Z}{Z_\odot} \right)^{-1} n_9^{-1} M_\odot \text{ yr}^{-1}$$

$$\dot{M}^{\text{ion}} k v_o \sim 2.7 \cdot 10^{35} L_{45} k v_{o,5000}^2 r_{1\text{pc}}^{-1} \left(\frac{Z}{Z_\odot} \right)^{-1} n_9^{-1} \text{ g cm s}^{-2}$$

$$\dot{\epsilon} \sim 6.6 \cdot 10^{43} L_{45} k^2 v_{o,5000}^3 r_{1\text{pc}}^{-1} \left(\frac{Z}{Z_\odot} \right)^{-1} n_9^{-1} \text{ erg s}^{-1}$$

where line luminosity, outflow velocity, radius, metallicity, and density have been normalized to $10^{45} \text{ erg s}^{-1}$, 5000 km s^{-1} , 1 pc , five times solar, and 10^9 cm^{-3} , in the same order.

Table 8 reports the values derived from the outflow parameters using the equations above. The value of $k = 5$ for C IV is the ratio of the v measured on the profile and the expected terminal velocity according to the simple model of Netzer & Marziani (2010). It is plausible that the emitting gas is still subject to acceleration by strong radiation forces within the BLR. In contrast, in the case of [O III], assuming that the emission is due to gas expelled from the nucleus, both the kinetic power and thrust are dissipated as the material traverses greater distances towards the outer regions of the AGN, beyond the influence of the central black hole gravitational pull. The alternative is that [O III] is emitted by the host galaxy gas. In this case, the [O III] emitting gas in outflow would reflect the radiative feedback of the AGN. In either case, the observations imply a notable difference in the outflow conditions between C IV and [O III] emission lines.

The estimations based on C IV $\lambda 1549$ suggest that in highly luminous quasars, the mechanical feedback estimated from mildly ionized gas (which is part of the multi-frequency outflows observed in powerful quasars) may be already close to achieve the required effect for evolutionary feedback on the host galaxy. The average ratio between the kinetic power of the C IV $\lambda 1549$ outflow is $|\dot{\epsilon}| \approx 0.04$, close to the value expected from theoretical models, 5% of the bolometric luminosity needed to account for the black hole mass - velocity dispersion correlation and host-spheroid co-evolution (e.g., Di Matteo et al. 2005). Effect on circum-nuclear and bulge star formation are expected to occur at a much lower threshold, $\dot{E}_{\text{kin}}/L_{\text{bol}} \sim 5 \times 10^{-3}$ (Hopkins et al. 2010; Hopkins & Elvis 2010).

6.3 Metal enrichment

The availability of the strongest UV lines, along with the emission features in the H β spectral range make it possible to estimate the metal content of the line emitting gas (Florin et al. 2024). Here we follow the methodology already tested in several recent works (Śniegowska et al. 2020; Garnica et al. 2022). An advantage with respect to them is the measurement of the Mg II, along with H β and the Fe II $_{\text{opt}}$.

We utilize 10 diagnostic ratios, namely: C IV/He II $\lambda 1640$, Si IV+O IV/He II, Si IV+O IV/C IV, C III $\lambda 1909$ /C IV, Al III/C IV, Al III/Si III $\lambda 1892$, Si III $\lambda 1892$ /C III $\lambda 1909$, Mg II/C IV, Fe II $\lambda 4570$ /H β , Al III/He II, avoiding Mg II/H β and C IV/H β that might be affected by the non-simultaneity of the observations. This set of ratios is available for 3 objects. For J2018 the Mg II is not available. We exclude J0934 and J1054 for which the 1400 blend is not observable. We seek the model that yields the minimum χ^2 between observed and predicted diagnostic ratios, in a grid of photoionization models covering the parameter space n_{H} , U with a step of 0.25 dex, and for 12 Z values between 0.01 and 1000 solar. We define the χ^2 as:

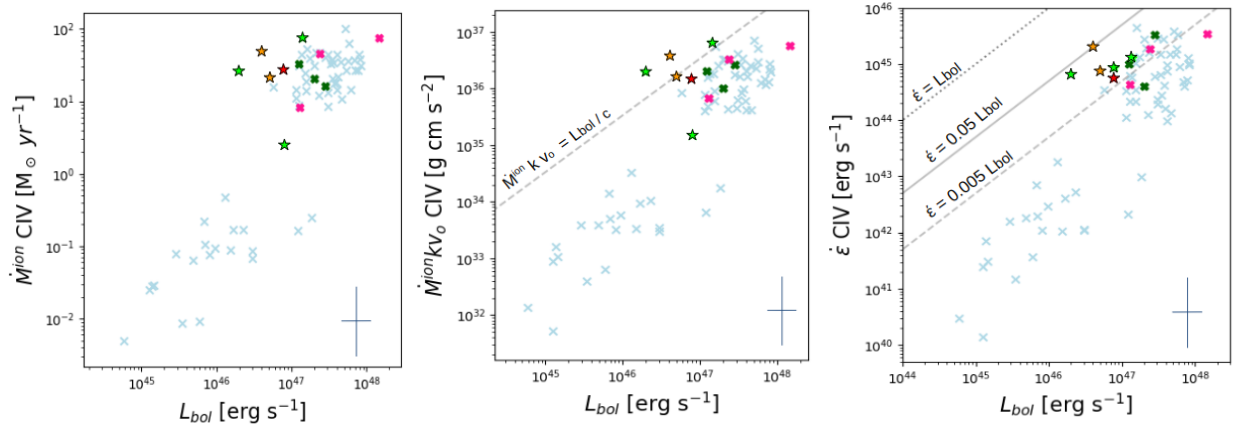


Figure 8. Distribution of the mass outflow rate (left), thrust (middle), and kinetic power (right) vs. bolometric luminosity for the C IV $\lambda 1549$ emission line. Black dotted, continuous and dashed lines show $\epsilon = L_{\text{bol}}$, $\epsilon = 0.05 L_{\text{bol}}$, and $\epsilon = 0.005 L_{\text{bol}}$, respectively. The crosses correspond to data extracted from [Deconto-Machado et al. \(2024\)](#), and stars for the sources of this work. Color scheme for [Deconto-Machado et al. \(2024\)](#) sources: light blue (Pop. A), green (bonafide Pop. xA), and pink (Pop. xA). Color scheme for the LBT sample: red (Pop. A), orange (bonafide xA), and lime (Pop. xA). Error bars are the typical uncertainties.

Table 8. Outflow physical parameters derived for C IV: mass of ionized gas, mass outflow rate, thrust and kinetic power

SDSS ID	M_{BH}	v_o	L_{CIV}	M^{ion}	\dot{M}^{ion}	$\dot{M}^{\text{ion}} k v_o$	ϵ
(1)	± 1.17	± 1712	± 0.21	± 66	± 17	± 2.26	± 0.332
(1)	(2)	(3)	(4)	(5)	(6)	(7)	(8)
J084502	2.29	-11293	44.52	165	50	3.81	2.106
J093403*	3.44	-8753	43.47	15	13	0.15	0.863
J105427	1.49	-11410	44.19	78	22	1.67	0.774
J125914	0.44	-8257	44.52	167	28	1.54	0.554
J144218	0.60	-10846	44.13	67	27	1.97	0.669
J210831	2.49	-12741	44.90	395	77	6.58	1.305

Notes: All measurements are in the quasar rest-frame. Columns: (1) SDSS identification. (2): black hole mass obtained with $H\beta$, in units of $\times 10^9 M_{\odot}$. (3): final outflow velocity (following the definition by [Deconto-Machado et al. 2024](#)), in units of km s^{-1} . (4) Logarithm of the line luminosity, in units of ergs s^{-1} . (5): mass of the ionized gas, in units of M_{\odot} . (6) mass outflow rate, in units of $M_{\odot} \text{ yr}^{-1}$. (7): thrust, in units of $\times 10^{37} \text{ g cm s}^{-2}$. (8): kinetic power, in units of $\times 10^{45} \text{ ergs s}^{-1}$. *Source showing broad absorption lines in C IV $\lambda 1549$ and Si IV $\lambda 1397$.

$$\chi^2(n_{\text{H}}, U, Z) = \sum_k w_k \frac{(R_{\text{obs},k} - R_{\text{CLOUDY},k})^2}{R_{\text{obs},k}^2}$$

where $R_{\text{CLOUDY},k}$ identifies each diagnostic ratio computed with CLOUDY 23.01 ([Gunasekera et al. 2023](#)), for a SED appropriate for xA sources. The weight w_k has been assumed equal 1 save in one case (J2108), where a larger weight has been given to Fe II emission. The metallicity estimates are summarized in Table 9. Four cases with the same SED were considered, based on different turbulence values: $t = 0 \text{ km s}^{-1}$, $t = 20 \text{ km s}^{-1}$, $t = 300 \text{ km s}^{-1}$. Fig. 9 shows the tight constraints in the parameter space n_{H} , U , Z for J0845. The values are consistent with previous estimates for high luminosity quasars at intermediate z , 10 – 20 times the solar values ([Hamann & Ferland 1993, 1999](#); [Dietrich et al. 2003](#); [Xu et al. 2018](#); [Śniegowska et al. 2021](#); [Garnica et al. 2022](#)), as well as for xA sources at low redshift and luminosity ([Florin et al. 2024](#)). If we take a prudential value, $Z \sim 10Z_{\odot}$, as a reference, the mass outflow rate of metals is very high $\dot{M}_{\text{metals}} \sim (50 \cdot 0.15) M_{\odot} \text{ yr}^{-1} \sim 10 M_{\odot} \text{ yr}^{-1}$.

The most intriguing case is perhaps the one of J210831. This source shows a spectrum where all the relative intensities of the broad components converge toward a scenario of high metallicity, along with low ionization and high density. The low ionization is suggested by the almost complete displacement toward the blue of

the Si IV and C IV lines, implying low values of all the ratios normalizing C IV $\lambda 1549$. The R_{FeII} values is the highest in our sample, and Al III $\lambda 1860$ is also very prominent. The O I and Si II blend is almost as strong as the 1400 Å blend. These indicators converge toward extreme solutions ([Negrete et al. 2012](#); [Martínez-Aldama et al. 2018](#)). However, the derived metallicity value is extremely high, implying that both the relative abundances and mass fraction are dominated by metals and that the BLR are strongly polluted through selective enrichment that may yield a chemical composition different from the solar one ([Wang et al. 2023](#)). The scaling of ~ 500 times the solar metallicity should therefore be viewed with extreme care. The introduction of thermal broadening (i.e., a turbulent velocity dispersion of 20 km s^{-1} and 300 km s^{-1} ([Temple et al. 2020, 2021](#)) in the CLOUDY simulations is not changing the very high metallicity values which remain extreme. The main consequence of the higher turbulence ($t = 300 \text{ km s}^{-1}$) is a widening of the confidence range i.e., to somehow “disperse” the result. However, if we impose a higher weight on the R_{FeII} ratio in the computation of the χ^2 , the metallicity of J2108 is reduced to $Z \sim 50Z_{\odot}$, consistent with the values derived for the most extreme xA sources ([Garnica et al. 2022](#)). This emphasizes the importance of involving high S/N data (higher S/N than the ones of the spectra in the present paper) that would permit a more precise decomposition of the blended line profiles, as well as the largest possible number of ratios, possibly given different

weight according to the accuracy of the measurements to compute of a minimum χ^2 that is representative of the best agreement between observed spectrum and model predictions.

In conclusion, the metallicity values are consistent with the values of the previous works which derived $\gtrsim 10Z_\odot$ for super-Eddington quasars. This conclusion is reinforced by the stability of the estimates with respect to changes in line broadening. This is not to say that all quasars have BLR chemical composition with super-solar abundance. On the converse, type-1 AGN apparently show a well-defined trends along the quasar main-sequence, also involving slightly sub-solar metallicities ($Z \sim 0.1 - 0.5Z_\odot$, Floris et al. 2024).

6.4 Hubble diagram

These physical conditions for xA quasars: (1) Eddington ratio constant or close to the Eddington limit, (2) black hole mass expressed in terms of virial motions and (3) spectral invariance, so that the product ionization parameter times density has to be approximately constant, make it possible to write the following equation that yield a redshift-independent luminosity (Marziani & Sulentic 2014):

$$\begin{aligned} L(\text{FWHM}) &= \mathcal{L}_0 \cdot (\text{FWHM})_{1000}^4 \\ &= 7.88 \cdot 10^{44} \left(\frac{L}{L_{\text{Edd}}} \right)^2 \cdot \frac{\kappa_{i,0.5} f_{S,2}^2}{h \bar{v}_{i,100\text{eV}}} \\ &\cdot \frac{1}{(n_H U)_{10^{9.6}}} (\text{FWHM})_{1000}^4 \text{ erg s}^{-1} \end{aligned}$$

where the energy value has been normalized to 100 eV ($\bar{v}_{i,100\text{eV}} \approx 2.42 \cdot 10^{16}$ Hz), $\kappa_{i,0.5}$ is the fraction of bolometric luminosity belonging to the ionizing continuum scaled to 0.5, the product $(n_H U)$ has been scaled to the typical value $10^{9.6} \text{ cm}^{-3}$, and the FWHM of the $\text{H}\beta$ BC is expressed in units of 1000 km s^{-1} . The FWHM of $\text{H}\beta$ broad component and of $\text{AlIII}\lambda 1860$ are hereafter adopted as a virial broadening estimator. Eq. 4 implies that, by a simple measurement of the FWHM of a LIL, one can derive a z -independent estimate of the accretion luminosity (Marziani & Sulentic 2014, c.f. Teerikorpi 2005).

The distance modulus μ computed from the virial equation, $L(\delta v)$, can be written as:

$$\mu = 2.5 [\log L(\delta v) - BC] - 2.5 \log(f_{\lambda\lambda}) - 2.5 \log(4\pi\delta_{10\text{pc}}^2) + 5 \cdot \log(1+z) \quad (4)$$

where the constant $-2.5 \log(4\pi\delta_{10\text{pc}}^2) = -100.19$, with $\delta_{10\text{pc}} \approx 3.08 \cdot 10^{19}$ the distance of 10 pc expressed in cm. The $f_{\lambda\lambda}$ can be the flux at 5100 \AA for the $\text{H}\beta$ sample, or the flux at 1700 \AA if the $\delta v = \text{FWHM}$ comes from the $\text{AlIII}\lambda 1860$ and $\text{SiIII}\lambda 1892$ lines (Dultzin et al. 2020).

Two of the six targets observed with the LBT fully meet the criterion defining xA sources ($R_{\text{FeII}} \gtrsim 1$); three of them can be considered bona-fide borderline xA, and one of them, J125914, a Pop. A but not meeting the xA selection criterion.

The Figure 10 shows the Hubble diagram μ versus z for several samples for which μ has been derived from $\text{FWHM}(\text{H}\beta)$. The 5 objects analyzed in the present work are shown by larger symbols in Figure 10 (black xA, gray borderline). It is notable that the two xA quasars closely agree with the prediction of standard cosmology and with the determinations from other samples. The averages of μ over redshift bins from 0 to ≈ 2.6 (Figure 10, right panels) for all determinations shown individually in the left panels) is following the

trend expected for standard cosmology with some small deviations. The agreement between the distance moduli estimated from the line width and the ones derived from standard cosmology is a restatement of a few basic aspects of the LIL emitting regions: a virial velocity field dominated by the central black hole mass, a scaling of the emitting region radius proportional to the square root of luminosity (to preserve spectral invariance), and of extreme Eddington ratios (Table 7 reports $L/L_{\text{Edd}} \gtrsim 1$). These conditions imply an increase of FWHM with $L^{1/4}$ (Marziani et al. 2022), or $L \propto \text{FWHM}^4$ (Marziani & Sulentic 2014). Clearly, more high quality, NIR observations – such as the ones collected with LBT – of the $\text{H}\beta$ spectral range for quasars at redshift $z \gtrsim 1$ are needed to test the possibility of using the the distance moduli estimated from the line width as distance indicators.

7 SUMMARY AND CONCLUSIONS

The main results of the investigation can be summarized as follows:

- We presented new LUCI observations at the LBT covering a sample of 6 highly accreting quasars (super-Eddington candidates) at $z \sim 2$. The NIR spectrographic camera LUCI allowed us to cover the $\text{H}\beta$ spectral region which yields a wealth of diagnostic information on the physical condition and dynamics of the line emitting region. SDSS spectra were used to analyze the spectral region of the UV emission lines from $\text{SiIV}\lambda 1397 + \text{OIV}\lambda 1402$ to $\text{MgII}\lambda 2800$.
- We carried out the data reduction of the original LUCI observations to ensure to maximize the S/N of the extracted spectra.
- The bolometric luminosity of the sample source is very high, $\log L_{\text{bol}} \gtrsim 47$ [erg s^{-1}], close to the domain of the WISE/SDSS selected hyper-luminous (WISSH) (Bischetti et al. 2017) and HEMS surveys (Marziani et al. 2009). The Eddington ratio is close to one, with average $\log L/L_{\text{Edd}} \sim -0.1 \pm 0.1$ (≈ 0 if the outlier J125914 is excluded), confirms the high radiative output of the sample sources.
- We considered the cross match between optical and UV selection criteria for the identification of xA sources. Two sources are bonafide xA sources, three can be considered borderline xA, and one of them is a Pop. A quasar.
- A multi-component fitting of the most prominent broad emission lines in the UV-optical ranges: 1400\AA blend, $\text{CIV}\lambda 1549$, 1900\AA blend, $\text{MgII}\lambda 2800$, and $\text{H}\beta$, permitted us to isolated a symmetric and unshifted component, strong in the low ionization lines, along with a blueshifted component associated with a strong outflow dominating the emission of the high ionization lines. The high amplitude $\text{CIV}\lambda 1549$ blueshifts $v \lesssim -2000 \text{ km s}^{-1}$ is detected in five sources out of six, all the super-Eddington candidates of the LBT sample.
- Blueshifts are higher amplitudes in the lines ($\text{CIV}\lambda 1549$, $\text{HeII}\lambda 1640$, $\text{SiIV}\lambda 1397$) whose parent species are of higher ionization potential.
- At the same time, $\text{H}\beta$, and $\text{MgII}\lambda 2800$ appear to be almost symmetric and unshifted or only marginally shifted. The intermediate ionization doublet $\text{AlIII}\lambda 1860$ shows modest shifts more consistent with the low-ionization lines. In larger samples, $\text{AlIII}\lambda 1860$ large shifts have been revealed although at a low prevalence (Marziani et al. 2022; Buendia-Rios et al. 2023). Their absence might be a consequence of the small sample size.

Several additional results are implied by the xA physical parameter estimates.

- Estimates of the outflow dynamical parameters (mass of ionized gas, mass outflow rate, thrust and kinetic power) were made using the CIV and $[\text{OIII}]$ emission lines. The wind parameter derived from the

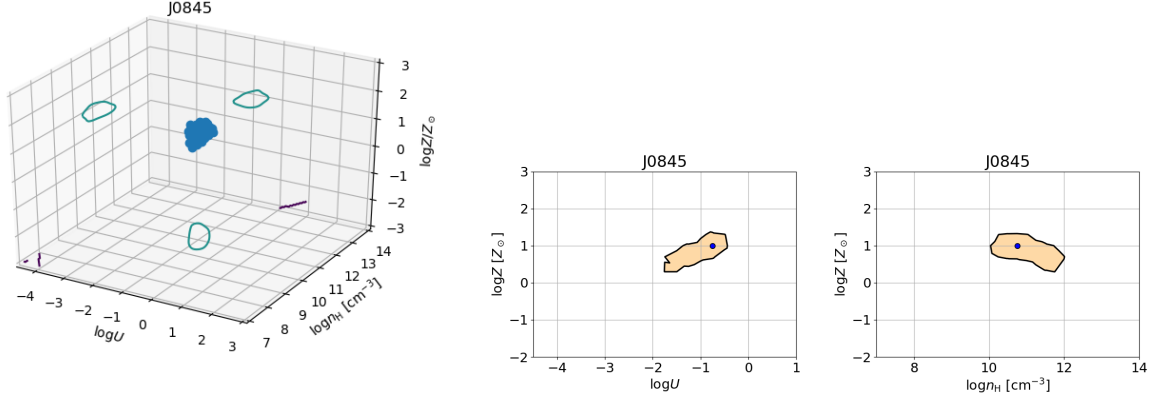


Figure 9. Parameter space n_H , U , Z for J084502. Left: data points in 3D space are elements in the grid of the parameter space selected for not being different from χ^2_{\min} by more than 1σ confidence level, for the case turbulence $t = 0 \text{ km s}^{-1}$. Middle: projections on the plane $(\log U, \log Z)$. Right: projections on the plane $\log n_H, \log Z$. The blue point marks the minimum χ^2 , and the contour delimits the 1σ confidence range.

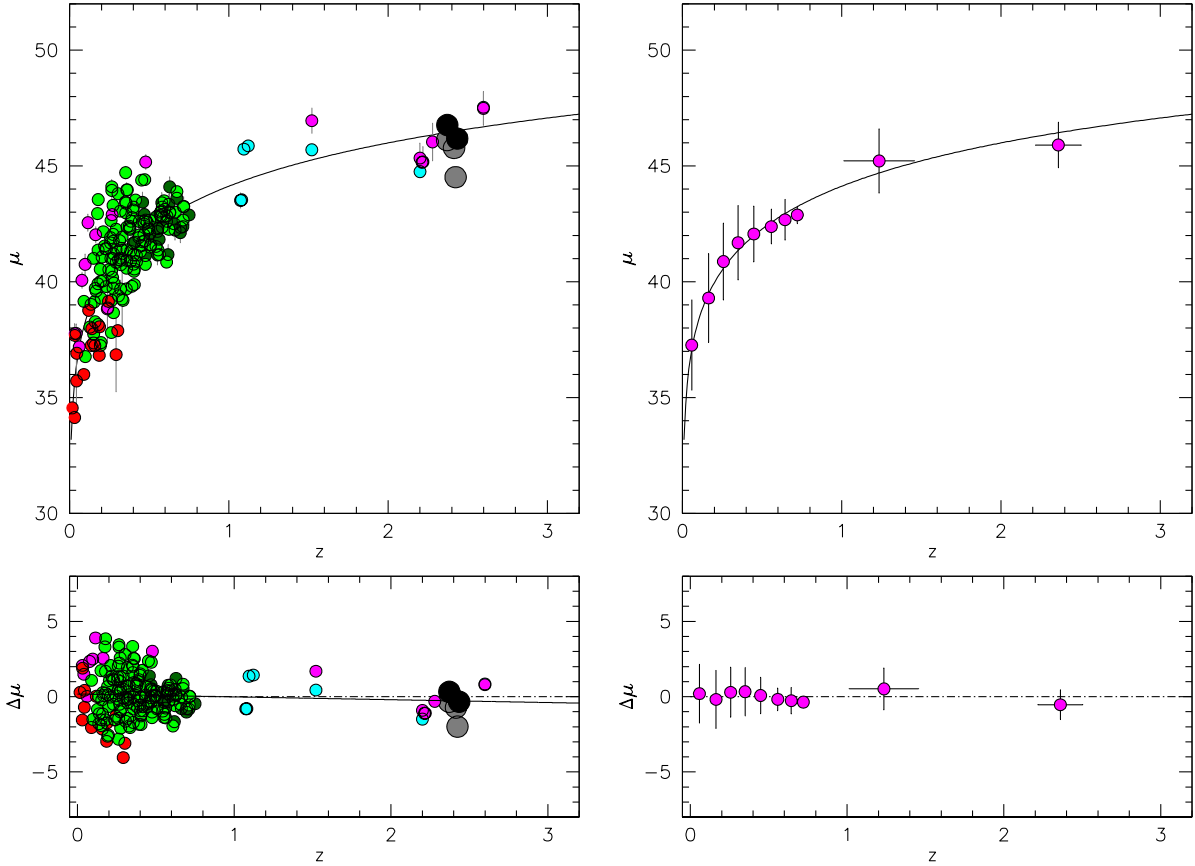


Figure 10. Left: Hubble diagram distance modulus μ versus redshift z obtained from the virial luminosity equation. The five sources that are classified as xA (black) or borderline xA (gray) considered in this study are shown by larger symbols. Samples in [Dultzin et al. \(2020\)](#) are included: red [Du et al. \(2016\)](#), green [Negrete et al. \(2018\)](#), dark green [Marziani et al. \(2013a\)](#). Cyan data points represents the xA quasars of the Hamburg-ESO Marziani-Sulentic (HEMS) survey ([Marziani et al. 2009](#)), magenta the sample of [Marziani et al. \(2022\)](#). Right: same as for the left panel, but with μ averaged over 10 redshift ranges. Lines: least-square on the residuals (gray) and Λ CDM cosmology model (black).

Table 9. Metal content estimates.

Ident.	$t = 0 \text{ km s}^{-1}$			$t = 20 \text{ km s}^{-1}$			$t = 300 \text{ km s}^{-1a}$			$t = 300 \text{ km s}^{-1}$		
	log Z [Z _⊙]	1 σ range [Z _⊙]	χ^2_{\min}	log Z [Z _⊙]	1 σ range [Z _⊙]	χ^2_{\min}	log Z [Z _⊙]	1 σ range [Z _⊙]	χ^2_{\min}	log Z [Z _⊙]	1 σ range [Z _⊙]	χ^2_{\min}
J084502	1.0	0.3 – 1.3	2.66	1.0	0.3 – 1.3	2.445	1.0	0.7 – 1.3	3.735	0.7	0.0 – 2.0	2.840
J125914	1.3	1.0 – 1.3	2.815	1.3	1.0 – 2.0	1.992	0.7	0.3 – 2.0	3.214	1.3	1.3 – 2.0	2.027
J144218	1.0:	-1.0 – 1.7	4.372	1.3	0.0 – 1.3	3.416	1.3	0.0 – 3.0	6.776	1.3	0.0 – 2.0	3.864
J210831 ^b	2.7	2.0 – 3.0	1.268	3.0	3.0 – 3.0	0.939	1.7	1.7 – 2.0	6.565	3.0	2.7 – 3.0	2.159

Notes: Columns are log Z, 1 σ confidence range in Z, minimum χ^2 in this order. ^a: case with higher weight to the FeII/H β ratio, otherwise identical to the other case with turbulence $t = 300 \text{ km s}^{-1}$. ^b J2108: no MgII. Double colon indicates poor constraints i.e., a wide 1 σ range ($2 \times \sigma_{\log Z} \gtrsim 2$).

blueshifted C IV $\lambda 1549$ emission have kinetic power close to the one needed to account for host galaxy and black hole coevolution. Since AGN winds are multi-frequency (e.g., Laha et al. 2021; Chartas et al. 2021; Kharb & Silpa 2023; Gianolli et al. 2024), it appears likely that the “bolometric” kinetic power may indeed be able to exert the feedback effect expected to drive the M_{BH} – host galaxy velocity dispersion correlation.

- The coverage of the UV and optical spectral ranges provided the measurements for $\sim 10 - 12$ diagnostic ratios suitable for the measurement of the metallicity of the broad line emitting gas. We confirm the high metallicity already found for xA systems at low- and high-luminosity (Floris et al. 2024, and references therein).

- Finally, we applied the virial luminosity equation to build the Hubble diagram for a sample of xA sources. We added 5 genuine xA with the luminosity estimated from the line width of H β . The results are consistent with the standard Λ CDM cosmology (D’Onofrio et al. 2024). More than of any cosmological implication, the Hubble diagram yields a representation of the virialized nature of the low-ionization emission preserved even in extreme quasars.

In conclusion, the LBT spectra of the H β rest frame range allowed us to consider several properties of super-Eddington candidates, already analyzed for sources selected from the $R_{\text{FeII}} \gtrsim 1$ criterion, as well as to achieve a proper estimation of the AGN outflow parameters by accurately measuring the redshift quasar redshift, confirming the possibility of significant feedback. In addition, even if the sample included only 5 extreme quasars, the agreement of their H β line widths with cosmological expectations, and the absence of significant shifts signaling strong wind effects, indicate that larger H β samples may one day turn useful for an independent estimation of the cosmological parameters.

ACKNOWLEDGEMENTS

D. Dultzin and C. A. Negrete acknowledge the support form grant IN111422 PAPIIT UNAM. C. A. Negrete acknowledges the support form CONACyT project Paradigmas y Controversias de la Ciencia 2022-320020, CONACyT CBF2023-2024-1418, PAPIIT IA104325 and IN119123. The work of T. M. Buendia-Rios has been sponsored by CONACyT-Mexico through the Ph.D. scholarship No. 760641. T. M. B.-R. acknowledges the hospitality and support of INAF – Astronomical Observatory of Padova where part of this work was done. This publication makes use of data products from the Two Micron All Sky Survey, which is a joint project of the University of Massachusetts and the Infrared Processing and Analysis Center/California Institute of Technology, funded by the National Aeronautics and Space Administration and the National Science Foundation. This publication used the facilities of the Italian Center for

Astronomical Archive (IA2) operated by INAF at the Astronomical Observatory of Trieste.

The LBT is an international collaboration among institutions in the United States, Italy, and Germany. LBT Corporation partners are: The University of Arizona on behalf of the Arizona university system; Istituto Nazionale di Astrofisica, Italy; LBT Beteiligungsgesellschaft, Germany, representing the Max-Planck Society, the Astrophysical Institute Potsdam, and Heidelberg University; The Ohio State University, and The Research Corporation, on behalf of The University of Notre Dame, University of Minnesota and University of Virginia.

DATA AVAILABILITY

IR spectra in ASCII format are provided as part of the paper. For each spectrum, the rest frame wavelength and specific flux are reported in units of \AA and $10^{-17} \text{ erg s}^{-1} \text{ cm}^{-2} \text{ \AA}^{-1}$, respectively.

Optical spectra are from the SDSS and can be downloaded from the data server of the SDSS Data Release 18.

REFERENCES

- Bischetti M., et al., 2017, *A&A*, **598**, A122
 Bisogni S., di Serego Alighieri S., Goldoni P., Ho L. C., Marconi A., Ponti G., Risaliti G., 2017, preprint, ([arXiv:1702.08046](https://arxiv.org/abs/1702.08046))
 Bon N., Marziani P., Bon E., Negrete C. A., Dultzin D., del Olmo A., D’Onofrio M., Martínez-Aldama M. L., 2020, *A&A*, **635**, A151
 Bonzini M., et al., 2015, *MNRAS*, **453**, 1079
 Boroson T. A., Green R. F., 1992, *ApJS*, **80**, 109
 Brotherton M. S., Runnoe J. C., Shang Z., DiPompeo M. A., 2015, *MNRAS*, **451**, 1290
 Bruhweiler F., Verner E., 2008, *ApJ*, **675**, 83
 Buendia-Rios T. M., Negrete C. A., Marziani P., Dultzin D., 2023, *A&A*, **669**, A135
 Caccianiga A., et al., 2015, *MNRAS*, **451**, 1795
 Cano-Díaz M., Maiolino R., Marconi A., Netzer H., Shemmer O., Cresci G., 2012, *A&A*, **537**, L8
 Capellupo D. M., Netzer H., Lira P., Trakhtenbrot B., Mejía-Restrepo J., 2016, *MNRAS*, **460**, 212
 Chartas G., et al., 2021, *ApJ*, **920**, 24
 Coatman L., Hewett P. C., Banerji M., Richards G. T., 2016, *MNRAS*, **461**, 647
 Conselice C. J., 2014, *ARA&A*, **52**, 291
 D’Onofrio M., Marziani P., Chiosi C., Negrete C. A., 2024, *Universe*, **10**, 254
 Deconto-Machado A., del Olmo Orozco A., Marziani P., Perea J., Stirpe G. M., 2023, *A&A*, **669**, A83
 Deconto-Machado A., del Olmo A., Marziani P., 2024, *arXiv e-prints*, p. [arXiv:2408.06260](https://arxiv.org/abs/2408.06260)
 Di Matteo T., Springel V., Hernquist L., 2005, *Nature*, **433**, 604

- Dietrich M., Hamann F., Shields J. C., Constantin A., Heidt J., Jäger K., Vestergaard M., Wagner S. J., 2003, *ApJ*, **589**, 722
- Dimitrijević M. S., Popović L. Č., Kovačević J., Dačić M., Ilić D., 2007, *MNRAS*, **374**, 1181
- Du P., Wang J.-M., 2019, *ApJ*, **886**, 42
- Du P., Wang J.-M., Hu C., Ho L. C., Li Y.-R., Bai J.-M., 2016, *ApJL*, **818**, L14
- Dultzin D., et al., 2020, *Frontiers in Astronomy and Space Sciences*, **6**, 80
- Duras F., et al., 2017, *A&A*, **604**, A67
- Duras F., et al., 2020, *A&A*, **636**, A73
- Elitzur M., Ho L. C., Trump J. R., 2014, *MNRAS*, **438**, 3340
- Elvis M., 2000, *ApJ*, **545**, 63
- Emmering R. T., Blandford R. D., Shlosman I., 1992, *ApJ*, **385**, 460
- Eracleous M., Halpern J. P., 2004, *ApJS*, **150**, 181
- Fabian A. C., 2012, *ARA&A*, **50**, 455
- Fiore F., et al., 2017, *A&A*, **601**, A143
- Floris A., Marziani P., Panda S., Sniegowska M., D’Onofrio M., Deconto-Machado A., Del Olmo A., Czerny B., 2024, *arXiv e-prints*, p. [arXiv:2405.04456](https://arxiv.org/abs/2405.04456)
- Francis P. J., Hewett P. C., Foltz C. B., Chaffee F. H., Weymann R. J., Morris S. L., 1991, *ApJ*, **373**, 465
- Ganci V., Marziani P., D’Onofrio M., del Olmo A., Bon E., Bon N., Negrete C. A., 2019, *A&A*, **630**, A110
- Garnica K., Negrete C. A., Marziani P., Dultzin D., Sniegowska M., Panda S., 2022, *A&A*, **667**, A105
- Gianolli V. E., et al., 2024, *A&A*, **687**, A235
- Gillette J., Hamann F., 2024, *MNRAS*, **528**, 6425
- Gunasekera C. M., van Hoof P. A. M., Chatzikos M., Ferland G. J., 2023, *Research Notes of the American Astronomical Society*, **7**, 246
- Hamann F., Ferland G., 1993, *ApJ*, **418**, 11
- Hamann F., Ferland G., 1999, *ARA&A*, **37**, 487
- Hartig G. F., Baldwin J. A., 1986, *ApJ*, **302**, 64
- Hewett P. C., Wild V., 2010, *MNRAS*, **405**, 2302
- Hopkins P. F., Elvis M., 2010, *MNRAS*, **401**, 7
- Hopkins P. F., Hernquist L., Cox T. J., Di Matteo T., Robertson B., Springel V., 2006, *ApJS*, **163**, 1
- Hopkins P. F., Bundy K., Hernquist L., Wuyts S., Cox T. J., 2010, *MNRAS*, **401**, 1099
- Johansson S., Zethson T., Hartman H., Ekberg J. O., Ishibashi K., Davidson K., Gull T., 2000, *A&A*, **361**, 977
- Kakkad D., et al., 2020, *A&A*, **642**, A147
- Kellermann K. I., Sramek R., Schmidt M., Shaffer D. B., Green R., 1989, *AJ*, **98**, 1195
- Kharb P., Silpa S., 2023, *Galaxies*, **11**, 27
- King A., Pounds K., 2015, *ARA&A*, **53**, 115
- Krawczyk C. M., Richards G. T., Mehta S. S., Vogeley M. S., Gallagher S. C., Leighly K. M., Ross N. P., Schneider D. P., 2013, *ApJS*, **206**, 4
- Kriss G., 1994, in Crabtree D. R., Hanisch R. J., Barnes J., eds, *Astronomical Society of the Pacific Conference Series Vol. 61, Astronomical Data Analysis Software and Systems III*. p. 437
- Kwan J., Cheng F.-Z., Fang L.-Z., Zheng W., Ge J., 1995, *ApJ*, **440**, 628
- Laha S., Reynolds C. S., Reeves J., Kriss G., Guainazzi M., Smith R., Veilleux S., Proga D., 2021, *Nature Astronomy*, **5**, 13
- Laor A., Fiore F., Elvis M., Wilkes B. J., McDowell J. C., 1997, *ApJ*, **477**, 93
- Leighly K. M., 2004, *ApJ*, **611**, 125
- Leighly K. M., Moore J. R., 2004, *ApJ*, **611**, 107
- Liu G., Zakamska N. L., Greene J. E., Nesvadba N. P. H., Liu X., 2013a, *MNRAS*, **430**, 2327
- Liu G., Zakamska N. L., Greene J. E., Nesvadba N. P. H., Liu X., 2013b, *MNRAS*, **436**, 2576
- Malkan M. A., Sargent W. L. W., 1982, *ApJ*, **254**, 22
- Martínez-Aldama M. L., Del Olmo A., Marziani P., Sulentic J. W., Negrete C. A., Dultzin D., Perea J., D’Onofrio M., 2018, *Frontiers in Astronomy and Space Sciences*, **4**, 65
- Marziani P., Sulentic J. W., 2012, *NewAR*, **56**, 49
- Marziani P., Sulentic J. W., 2014, *MNRAS*, **442**, 1211
- Marziani P., Sulentic J. W., Dultzin-Hacyan D., Calvani M., Moles M., 1996, *ApJS*, **104**, 37
- Marziani P., Sulentic J. W., Stirpe G. M., Zamfir S., Calvani M., 2009, *A&A*, **495**, 83
- Marziani P., Sulentic J. W., Plauchu-Frayn I., del Olmo A., 2013a, *AAp*, **555**, 89, 16pp
- Marziani P., Sulentic J. W., Plauchu-Frayn I., del Olmo A., 2013b, *ApJ*, **764**, 150
- Marziani P., Sulentic J. W., Negrete C. A., Dultzin D., D’Onofrio M., Del Olmo A., Martínez-Aldama M. L., 2014, *The Astronomical Review*, **9**, 6
- Marziani P., Martínez Carballo M. A., Sulentic J. W., Del Olmo A., Stirpe G. M., Dultzin D., 2016, *Ap&SS*, **361**, 29
- Marziani P., Negrete C. A., Dultzin D., Martínez-Aldama M. L., Del Olmo A., D’Onofrio M., Stirpe G. M., 2017, *Frontiers in Astronomy and Space Sciences*, **4**, 16
- Marziani P., et al., 2018a, *Frontiers in Astronomy and Space Sciences*, **5**, 6
- Marziani P., et al., 2018b, in *Revisiting narrow-line Seyfert 1 galaxies and their place in the Universe*. 9-13 April 2018. Padova Botanical Garden, Italy. Online at https://pos.sissa.it/cgi-bin/reader/conf.cgi?confid=328, id.2. SISSA/ISAS, p. 002 ([arXiv:1807.03003](https://arxiv.org/abs/1807.03003))
- Marziani P., et al., 2019, *A&A*, **627**, A88
- Marziani P., et al., 2021, *Research Notes of the American Astronomical Society*, **5**, 25
- Marziani P., et al., 2022, *ApJS*, **261**, 30
- Matthews B. M., et al., 2021, *ApJS*, **252**, 15
- Mediavilla E., Jiménez-Vicente J., Fian C., Muñoz J. A., Falco E., Motta V., Guerras E., 2018, *ApJ*, **862**, 104
- Mediavilla E., Jiménez-vicente J., Mejía-restrepo J., Motta V., Falco E., Muñoz J. A., Fian C., Guerras E., 2019, *ApJ*, **880**, 96
- Mejía-Restrepo J., Trakhtenbrot B., Lira P., Netzer H., Capellupo D., 2016, in *Active Galactic Nuclei: What’s in a Name?*. p. 7, [doi:10.5281/zenodo.60354](https://doi.org/10.5281/zenodo.60354)
- Mejía-Restrepo J. E., Lira P., Netzer H., Trakhtenbrot B., Capellupo D. M., 2018, *Nature Astronomy*, **2**, 63
- Mineshige S., Kawaguchi T., Takeuchi M., Hayashida K., 2000, *PASJ*, **52**, 499
- Moore C. E., 1945, *Contributions from the Princeton University Observatory*, **20**, 1
- Negrete C. A., Dultzin D., Marziani P., Sulentic J. W., 2012, *ApJ*, **757**, 62
- Negrete C. A., Dultzin D., Marziani P., Sulentic J. W., 2013, *ApJ*, **771**, 31
- Negrete C. A., et al., 2018, *A&A*, **620**, A118
- Netzer H., 2015, *ARA&A*, **53**, 365
- Netzer H., 2019, *MNRAS*, **488**, 5185
- Netzer H., Marziani P., 2010, *ApJ*, **724**, 318
- Netzer H., Lira P., Trakhtenbrot B., Shemmer O., Cury I., 2007, *ApJ*, **671**, 1256
- Netzer H., Lani C., Nordon R., Trakhtenbrot B., Lira P., Shemmer O., 2016, *ApJ*, **819**, 123
- Ohsuga K., Mineshige S., 2007, *ApJ*, **670**, 1283
- Ohsuga K., Mori M., Nakamoto T., Mineshige S., 2005, *ApJ*, **628**, 368
- Osterbrock D. E., Pogge R. W., 1985, *ApJ*, **297**, 166
- Pickles A. J., 1998, *PASP*, **110**, 863
- Proga D., 2007, in Ho L. C., Wang J. W., eds, *Astronomical Society of the Pacific Conference Series Vol. 373, The Central Engine of Active Galactic Nuclei*. p. 267 ([arXiv:astro-ph/0701100](https://arxiv.org/abs/astro-ph/0701100)), [doi:10.48550/arXiv.astro-ph/0701100](https://doi.org/10.48550/arXiv.astro-ph/0701100)
- Punsly B., Marziani P., Zhang S., Muzahid S., O’Dea C. P., 2016, *ApJ*, **830**, 104
- Richards G. T., et al., 2006, *AJ*, **131**, 2766
- Richards G. T., et al., 2011, *AJ*, **141**, 167
- Risaliti G., Elvis M., 2010, *A&A*, **516**, A89
- Rousselot P., Lidman C., Cuby J. G., Moreels G., Monnet G., 2000, *A&A*, **354**, 1134
- Sadowski A., 2011, *arXiv e-prints*, p. [arXiv:1108.0396](https://arxiv.org/abs/1108.0396)
- Sani E., Lutz D., Risaliti G., Netzer H., Gallo L. C., Trakhtenbrot B., Sturm E., Boller T., 2010, *MNRAS*, **403**, 1246
- Seifert W., et al., 2003, in Iye M., Moorwood A. F. M., eds, *Society of Photo-Optical Instrumentation Engineers (SPIE) Conference Series Vol. 4841*,

- Instrument Design and Performance for Optical/Infrared Ground-based Telescopes. pp 962–973, [doi:10.1117/12.459494](https://doi.org/10.1117/12.459494)
- Shankar F., Salucci P., Granato G. L., De Zotti G., Danese L., 2004, *MNRAS*, **354**, 1020
- Shankar F., Weinberg D. H., Miralda-Escudé J., 2009, *ApJ*, **690**, 20
- Shen Y., 2013, *Bulletin of the Astronomical Society of India*, **41**, 61
- Shen Y., 2016, *ApJ*, **817**, 55
- Shen Y., Ho L. C., 2014, *Nature*, **513**, 210
- Shen Y., Liu X., 2012, *ApJ*, **753**, 125
- Sigut T. A. A., Pradhan A. K., 1998, *ApJ*, **499**, L139
- Sigut T. A. A., Pradhan A. K., Nahar S. N., 2004, *ApJ*, **611**, 81
- Skrutskie M. F., et al., 2006, *AJ*, **131**, 1163
- Śniegowska M., Kozłowski S., Czerny B., Panda S., Hryniewicz K., 2020, *ApJ*, **900**, 64
- Śniegowska M., Marziani P., Czerny B., Panda S., Martínez-Aldama M. L., del Olmo A., D’Onofrio M., 2021, *ApJ*, **910**, 115
- Sulentic J. W., Marziani P., Dultzin-Hacyan D., 2000, *ARA&A*, **38**, 521
- Sulentic J. W., Bachev R., Marziani P., Negrete C. A., Dultzin D., 2007, *ApJ*, **666**, 757
- Sulentic J. W., et al., 2017, *A&A*, **608**, A122
- Teerikorpi P., 2005, ArXiv Astrophysics e-prints,
- Temple M. J., Ferland G. J., Rankine A. L., Hewett P. C., Badnell N. R., Ballance C. P., Del Zanna G., Dufresne R. P., 2020, *MNRAS*, **496**, 2565
- Temple M. J., Ferland G. J., Rankine A. L., Chatzikos M., Hewett P. C., 2021, *MNRAS*, **505**, 3247
- Temple M. J., et al., 2024, *MNRAS*, **532**, 424
- Tody D., 1986, in Crawford D. L., ed., Society of Photo-Optical Instrumentation Engineers (SPIE) Conference Series Vol. 627, Instrumentation in astronomy VI. p. 733, [doi:10.1117/12.968154](https://doi.org/10.1117/12.968154)
- Trakhtenbrot B., Netzer H., 2012, *MNRAS*, **427**, 3081
- Vanden Berk D. E., et al., 2001, *AJ*, **122**, 549
- Vestergaard M., Peterson B. M., 2006, *ApJ*, **641**, 689
- Vestergaard M., Wilkes B. J., 2001, *ApJS*, **134**, 1
- Vietri G., 2017, in American Astronomical Society Meeting Abstracts. p. 302.06
- Vietri G., et al., 2018, *A&A*, **617**, A81
- Vietri G., et al., 2020, *A&A*, **644**, A175
- Wandel A., Petrosian V., 1988, *ApJ*, **329**, L11
- Wang J.-M., et al., 2023, *ApJ*, **954**, 84
- Wills D., Netzer H., 1979, *ApJ*, **233**, 1
- Xu F., Bian F., Shen Y., Zuo W., Fan X., Zhu Z., 2018, *MNRAS*, **480**, 345
- Zamanov R., Marziani P., Sulentic J. W., Calvani M., Dultzin-Hacyan D., Bachev R., 2002, *ApJL*, **576**, L9
- Zamfir S., Sulentic J. W., Marziani P., 2008, *MNRAS*, **387**, 856

This paper has been typeset from a \LaTeX file prepared by the author.